INL/JOU-18-51979-Revision-0

On the Flow Induced Vibration of an Externally Excited Nuclear Reactor Experiment

Griffen Latimer, Wade R Marcum, Trevor K. Howard, Suyang Liu, Aaron Weiss, Musa Moussaoui, Colby B Jensen, Warren F Jones, Ann Marie Phillips, Nicolas E Woolstenhulme, Jed N Campbell

August 2018

INL/JOU-18-51979-Revision-0

On the Flow Induced Vibration of an Externally Excited Nuclear Reactor Experiment

Griffen Latimer, Wade R Marcum, Trevor K. Howard, Suyang Liu, Aaron Weiss, Musa Moussaoui, Colby B Jensen, Warren F Jones, Ann Marie Phillips, Nicolas E Woolstenhulme, Jed N Campbell

August 2018

Idaho National Laboratory
Idaho Falls, Idaho 83415

http://www.inl.gov

Prepared for the
U.S. Department of Energy
National Nuclear Security Administration
Under DOE Idaho Operations Office
Contract DE-AC07-05ID14517

HIGHLIGHTS

> An experiment study was performed on the vibrational response of a newly proposed design to be placed in the Advanced Test Reactor.

> The study utilizes compact triaxial accelerometers throughout the experimental apparatus.

> An assessment of data synthesis methods was performed and yielded a credible process laid out for such a study.

> The experimental data was compared against several semi-numerical models and shown to be well suited and safe in-design.

On the Flow Induced Vibration of an Externally Excited Nuclear Reactor Experiment

Griffen Latimer[a1], Wade R. Marcum[a,b,2], Trevor K. Howard[a], Warren Jones[b], Ann Marie Phillips[b], Nicolas Woolstenhulme[b], Suyang Liu[a], Aaron Weiss[a,] Jed Campbell[b], Musa Moussaoui[a], Colby Jensen[b]

[a] Oregon State University, School of Nuclear Science and Engineering
116 Radiation Center, Corvallis, OR 97330, United States

[b] Idaho National Laboratory, Nuclear Fuels & Materials Department
2525 Fremont Ave., Idaho Falls, ID, 83415

[1] Corresponding Author Contact Information:
Griffen Latimer
116 Radiation Center
Oregon State University
Corvallis OR 97331
P 541.737.2341
F 541.737.0480
E latimerg@oregonstate.edu

[2] Corresponding Author Contact Information:
Dr. Wade R. Marcum
Associate Professor
116 Radiation Center
Oregon State University
Corvallis OR 97331
P 541.737.2341
F 541.737.0480
E wade.marcum@oregonstate.edu

Submitted to *Nuclear Engineering and Design* as a full length article

May 6, 2018

ABSTRACT

An in-pile, drop-in experiment design is presently being designed and studied for the near-term deployment within the Advanced Test Reactor (ATR) located at the Idaho National Laboratory (INL); this experiment is termed the Miniplate-1 Large-B (MP-1 LB) Experiment. A number of explicit studies are performed during the design- and safety-related stage. Traditionally, a clear and logical methodology has been developed and utilized for analyses such as hydraulics, thermal-loads, mechanical loads, and others for these experiments. Recently a small component from a different experiment assembly mechanically separated while in the reactor's core. While this experiment didn't compromise the safety of the reactor, it led to a higher-level question which centered on whether the appropriate level of consideration was being made toward the fluid-structure-interactions of these experiments. The outcome yielded separate flow test experiments of like-for-like geometry in an experimental loop located at Oregon State University which produces experimental data compliant with applicable parts and requirements to ASME's NQA-1 2008, 2009a standard – suitable for benchmark evaluation. The objectives of this study are to (1) develop a process for handling and interpreting the mechanical response of the test elements during hydraulic testing, to (2) characterize the motion of a specific test element during a flow test which imposes a wide range of hydraulic conditions, and (3) provide objective observations toward the potential safety related implications that are tied to the synthesized data. The outcome of this study has led to a confident process in inspecting the experimental data, synthesized it for interpretation, identified several unique hydraulic characteristics of the experiment design which were previously unknown, and demonstrated that the likelihood for mechanical failure resulting from fluid-structure-interactions in the reactor is far below any criterion for concern of the element's safety.

1 INTRODUCTION

In most nuclear reactors, water is used as both a coolant and a moderator. As a moderator, it thermalizes neutrons to better facilitate the fission reaction; as a coolant, it removes heat from the surface of the fuel elements. Most reactors employ the use of rod-type fuel which in many cases has been extensively hydraulically tested and is thoroughly characterized. Less common is the use of plate-type fuel which benefits in the transfer of heat from having increased surface area to volume ratio, allowing for higher operating power density. One detriment from the plate-type geometry in high power density reactors arises from the need to have increased coolant velocities passing in the void space that separates each plate, most commonly referred to as a sub-channel. These sub-channels facilitate such flow conditions to remove the relatively large amount of heat produced within each respective fuel plate.

Currently, there are five high-performance research reactors (HPRRs) in the U.S. that employ both the use of plate type fuel and high enriched uranium (HEU) (~93% U-235 weight fraction). In an effort to reduce proliferation risk, these reactors are being converted to low enriched uranium (LEU) fuel (<20% U-235 weight fraction) through mandate of the U.S. Department of Energy [1]. At Oregon State University (OSU), thermal hydraulic testing is being performed on prototypic LEU fuel and mechanical surrogates for these reactors using the Hydro-Mechanical Fuel Test Facility (HMFTF) to support a large integrated program that intends on qualifying the LEU fuel for use and therefore provide a fuel which is suitable for conversion of the five U.S. HPRRs [2-4].

Of particular interest during flow testing is the characterization and quantification of the dynamic response of the test element when exposed to flow conditions. In a high-velocity flow field, the fluid-structure interactions (FSI) have been shown to be of relevance when understanding safety-related attributes of in-pile components. Therefore the structural response of the element within the flow field may lead to a coherent motion of the test element and could, under certain flow conditions, cause damage to the element. Understanding this motion is important in identifying possible wear locations due to continuous rubbing against the element's mating component surface – the flow simulator wall – or from excessive vibrations. Recent flow tests performed on conceptual elements that are planned to be placed in the Advanced Test Reactor (ATR) for long-term irradiation cycles included the use of high-resolution, tri-axes accelerometers which were attached at numerous locations on the test elements during testing within the HMFTF. The direct output of each of the tri-axis accelerometers was the acceleration that they experienced. In order to estimate and attempt to make credible observations on the motion path of the test elements, one must consider multiple aspects when synthesizing acceleration into position; a specific example includes the numerical integration scheme chosen for application. Limitations of noise-to-signal levels, acquisition rate, and acquisition duration all couple with the integration scheme chosen to detail a credible process for quantifying and characterizing the motion of the test element experienced during each respective flow test.

The objective of this study is to (1) develop a process for handling and interpreting the mechanical response of the test elements during hydraulic testing, to (2) characterize the motion of a specific test element during a flow test which imposes a wide range of hydraulic conditions, and (3) provide objective observations toward the potential safety related implications that are tied to the synthesized data.

The culmination of this work provides a greater understanding of the dynamic response of the test element for this specific case, but also creates the framework of a method which may be employed for future use on similar tests, along with recommendations and justifications for improvements which may further the ability to adequately capture the effects of flow-induced vibration of circular cylindrical structures, mainly in the application of nuclear reactor components.

2 SURVEY OF LITERATURE

Given the direct analytic relation between an object's acceleration and its explicit position, it is theoretically possible to reconstruct an object's position when a discrete acceleration signal is directly sampled. However, it must be assumed that the boundary conditions to relate the acceleration and position are known and the measurement of acceleration is sufficient in detail to reconstruct the displacement.

Double integration of accelerometer data was investigated thoroughly in a number of studies by Ribeiro et al. [5-10] to calculate the displacement and thus the stresses in large structures. Accelerometers proved to be invaluable due to their low cost and in their ability to easily mount to any surface. LVDTs, though providing a direct output of displacement, are difficult in their implementation since they are non-inertial and thus require a fixed reference frame.

Early attempts were made at using an analog integrating circuit, to directly measure displacement from the output of an accelerometer [9]. The circuit consisted of an input charge amplifier, low-pass filter, integrator amplifier, and output amplifier. The resulting displacements from the accelerometer were compared to the true displacement as measured by an LVDT, and resulted in errors of 100, 200, and 300 percent in three separate tests. These large errors were due to vibration transients introducing an external force to the system in combination with the natural oscillatory response of the integrator. It was concluded that this method of double integration was not feasible unless the input signal was a steady sinusoid.

As an alternative to the analog integrator circuit, a digital integration method was proposed [10]. Theoretically, the acceleration $a(t)$, velocity $v(t)$, and displacement $d(t)$ will have a mean value of zero, but in practice it was shown that low-frequency components of the signal at and near DC (0 Hz) cause a shift in the data to have a non-zero mean. To attenuate this, a high-pass filter with a cutoff frequency of 1 Hz was proposed. The filter used was of the finite impulse response (FIR) type due to its inherent stability and linear phase response. The main problem with this method, however, was that there was significant aliasing of the system's response due to the inherent sample delay characteristic of FIR filters, which is undesirable, especially when the signal of interest can only be sampled for a short duration. Smith, et al. [11] proposed that aliasing and leakage are in fact a dual phenomenon; a frequency signal that is sampled to coarsely will cause the impulse response function to be distorted by aliasing in the time domain.

Later studies attempted to improve upon the digital filtering method by employing the use of a fast Fourier transform (FFT) for the direct digital integration (DDI) of the data, referred to as the FFT-DDI method [8]. The basic algorithm to this method is to first take the discrete Fourier transform (DFT) of the acceleration data, then manually attenuate the desired low-frequency content by setting all frequencies below a certain cutoff value equal to a constant. Then the inverse Fourier transform is taken of the real component of the signal to get the filtered acceleration data. This data is then numerically integrated to get velocity, after which the process is repeated again to get the filtered displacement data. Since the frequencies below the cutoff value are not entirely removed, the effect of time aliasing is not as pronounced as in the previous methods.

Another study [12] built off Ribeiro's work and analyzed the double integration technique for accelerometers using various digital filters; finite impulse response (FIR), infinite impulse response (IIR), and the fast Fourier transform (FFT). Finite impulse filters are advantageous in that they are inherently stable, have a linear phase response, and are non-recursive, thus they can be used in real-time. However, they have the disadvantage of having an inherent sample delay causing aliasing in the temporal domain, and they are more computationally expensive than other filter types, requiring a higher filter order for an equivalent frequency response. In contrast, IIR produce a much shorter sample delay than an FIR filter and are much less computationally expensive, however they are not always guaranteed to be stable, and do not always have a linear phase response [13, 14].

The FFT-DDI method was compared against the FIR and IIR filters in a laboratory application [12], and this method was selected as the ideal filter for their specific application due to its ability to closely match the true displacement output as measured by an LVDT, even under relatively noisy conditions; this was performed various ways by altering sampling methods and inserting artificial noise. The results indicated that the method proved to be robust, with errors of no more than ten percent of true measured value.

Arraigada performed a study comparing the vibrational response of a piezoelectric and micro-electrical mechanical system (MEMS) accelerometer in the application of road deflections due to rapid changes in loading [15]. Multiple trials were performed, changing the sampling rate of each accelerometer to determine the influence on the numerical double-integration process. Arraigada employed the trapezoidal integration scheme for the double-integration method, and did not use a high-pass or low-pass filter in order to preserve all frequency content from the sampled data. The main problem identified in the time integration was that the lower frequencies are amplified, the higher frequencies are reduced, and there is a 180-degree phase change. To correct for the accelerometer drift, Arraigada used a detrending approach by fitting the acceleration data with a high-order polynomial, which was then subtracted from the acceleration curve to remove the baseline drift. This method proved to provide a reliable correction to the drift and the results were in excellent agreement with the LVDT measured displacement history.

Various numerical methods used to integrate and differentiate discrete data have been developed in an attempt to quantify the instantaneous value of the derivative or antiderivative of a data set whose explicit function is unknown. One family of equations commonly used are referred to as the Newton-Cotes formulas. They comprise methods such as the trapezoidal rule, Simpson's rule, Simpson's 3/8 rule, and Boole's rule [16]. They are ideal for use when a coarsely sampled signal is known to behave well under a polynomial interpolation, which results in the formulation of a composite integral of increasing order for each method. Each method applies a weighting coefficient to the polynomial function in an attempt to better represent the true signal.

With an increased order integration scheme comes a complementary ability to approach that of a more contiguous solution form, however, this increased order accuracy also requires a larger number of discrete points to integrate across and therefore may result in the 'numerical smoothing' of data. This emphasizes the importance of sampling rate of a signal relative to the true response of the system; if a signal is sampled at a sufficiently high rate, then the higher-order methods may not be necessary. Conversely if the sampling rate is too low, then it may be necessary to form a composite integral by further interpolating the data with a spline function, or similar, in conjunction with using a higher-order Newton-Cotes formula. The criteria for determining whether or not the sampling rate is high enough will be specific to each application, and is sensitive to numerous factors including the total sample duration and the expected frequency response of the system such as the vibration of a circular cylindrical structure.

Flow-induced vibration (FIV), specifically that of circular cylindrical structures, is a phenomenon that was first quantified in 1878 by Czech physicist Vincenc Strouhal; he defined the non-dimensional cylinder shedding frequency known as the Strouhal number as

$$\mathrm{St} = \frac{fD}{U}, \tag{1}$$

where f is the vortex shedding frequency, D is the cylinder diameter, and U is the freestream velocity of the flow [17]. The typical value for the Strouhal number is taken as $\mathrm{St} \approx 0.2$ which is valid for flows with a Reynolds number between about 10^2 and 10^5. The Reynolds number is defined as

$$\mathrm{Re} = \frac{UD}{\nu} \tag{2}$$

where ν is the kinematic viscosity. The Reynolds number is a dimensionless parameter which describes the relative importance of inertial and viscous effects in a flow, and may be used to classify the flow as either laminar or turbulent.

Flow-induced vibration is certainly not specific to the nuclear industry, however the relative safety impact of failures due to FIV in nuclear reactors places specific importance on this application. Flow-induced vibration was first experienced in the nuclear power reactor fleet in 1963, with the Fermi-1 liquid metal fast breeder reactor, where 45 steam generator tubes failed within the first 55 days of operation due to FIV from the liquid sodium coolant [18]. More recently, in 2010, FIV was the primary failure mechanism in the San Onofre Nuclear Generating Station, where improper manufacturing, handling, and replacement of the U-Tube steam generator resulted in failure shortly after its replacement [19]. Events such as these have made it evident that FIV is not just a secondary issue in the consideration of design and operation of mechanical equipment, but rather that of a primary concern on the basis of safety. As a result, many studies have been performed on the vibrational characteristics of structures analogous to the geometries and fluid environments in both research and power reactor space.

The basis of FIV requires a broader understand of the nature of fluid-structure interactions (FSI). If a solid body is immersed in a vibrating fluid, this will cause the structure to vibrate as well; some amount of the fluid will move in phase with the body while some of it will move out of phase with the body. This is the concept of hydrodynamic mass which was proposed by Friedrich

Bessel in 1828 based on his observation of the behavior of a swinging pendulum in fluid [20]. The fluid moving in phase will act to contribute to the mass of the body, hence the term hydrodynamic mass (also commonly referred to as virtual mass or added mass). If the body is subjected to an excitation force, *F*, then this is expressed mathematically as

$$\left(M_P + M_H\right)a + c_d v + kd = F \tag{3}$$

where (3) is analogous to solid-body motion except with the addition of the hydrodynamic mass, M_H, which is equivalent to

$$M_H = \rho_f V C_m. \tag{4}$$

In (4), ρ_f is the fluid density, V is the volume of the body, and C_m is the hydrodynamic mass coefficient. The relations shown in (3) and (4) represent the simplest case of a one-degree of freedom system, and cannot be used to describe the complete effects of the hydrodynamic mass in any real situation; the calculation of (4) is heavily dependent on geometry and frequency modes. The values of C_m for more common geometries are often tabulated in reference tables [21].

Some early studies have been performed by Fritz and Kiss [22]; first in 1966 on the vibration response of a cantilevered cylinder surrounded by an annular fluid. In this study, a solid aluminum cylinder was secured inside a sealed cylindrical shell, fastened to a shake table, and filled with water. The test element was subjected to varying forced vibrational amplitudes, and the response measured with multiple accelerometers and strain gages. In addition to the physical analysis, a theoretical model was created based on the fundamental equations of conservation of mass and momentum to compare with the measured frequency response of the test element; the results accurately predicted the natural frequency response of the cylinder in both air and water. In 1972, Fritz performed another study similar to the previous one [23], while extending the analysis from two-body motion with liquid coupling for concentric circular cylinders to a more broad analysis on multi-body motion with liquid coupling for various geometries. In addition to this, Fritz defines criteria for which one can mathematically justify using the simplifying assumption of inviscid and incompressible flow for the analytical calculation of frequency modes.

The dynamic behavior of shells was studied extensively by Flügge and Beskos [24, 25], who developed an equation of motion for circular cylindrical shells. A single shell in a static environment is simple to analyze, but the same method may be more rigorously applied to model the scenario of multiple coaxial shells conveying a viscous, compressible fluid. In the case of submerged shells, the interaction of the fluid and the solid will increase the radial stress on the shells, while acting to dampen vibrations.

Païdoussis has contributed a substantial amount of work in the field of FIV, with a large body of work on the vibration response of circular cylindrical shells containing fluids, including a large study on their stability conveying fluid [26-28]. He performed an early study investigating the phenomenon of flutter of both cantilevered and fixed shells with internal and external fluid flow; a new phenomenon was observed in which the shell loses stability in the second circumferential mode [29]. This highlighted an important difference between the vibrational response of a thick-walled and a thin-walled pipe; if a cylindrical pipe is sufficiently thin-walled, then it is considered to be a shell, but a thick-walled pipe may be considered a beam. It is known that the only form of instability in circular cylindrical beams is that of the lateral, or beam-type, modes; these occur in the first circumferential mode ($n = 1$). The consequence of a thin-walled shell is that in addition to the usual beam-type modes, the shell may also lose stability in a circumferential mode, like those shown in Fig. 1.

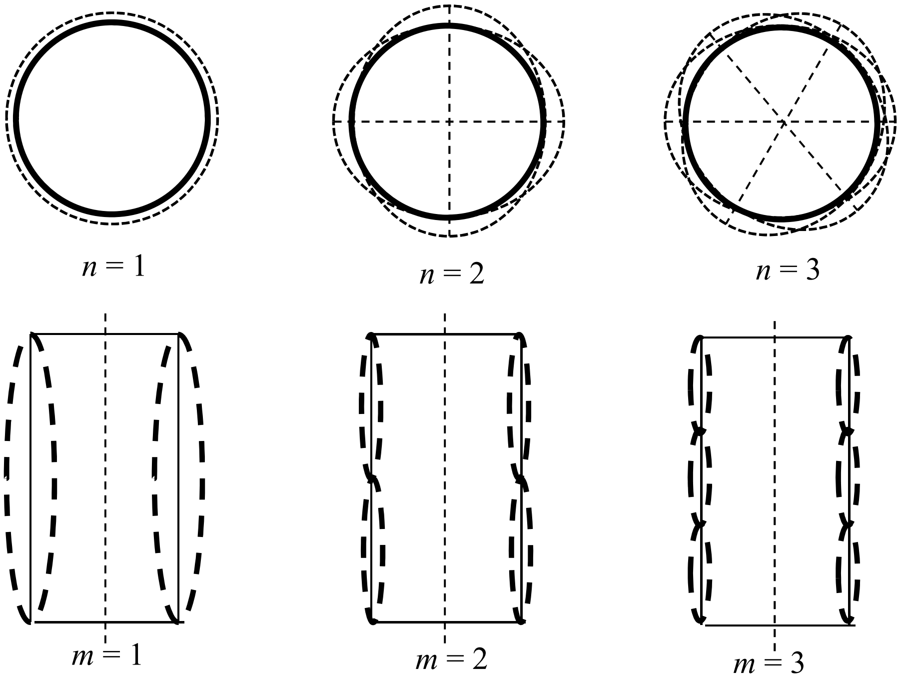

Fig. 1. First three circumferential (top) and axial (bottom) modes

Like many similar studies, Païdoussis developed his model in terms of Flügge's shell equations, in which the solution takes the form of a traveling wave along the axial and radial directions on the shell. The flow was assumed to be subsonic and potential, and in order to simplify the analysis, the shell was analyzed only up to the point of instability, to conserve a linear relation. The hydrodynamic mass is formulated in terms of the Bessel functions, and the problem was non-dimensionalized relative to the critical velocity, at which the shell loses stability. An experimental apparatus was designed to compare against the analytical model, and the results were shown to be in qualitative agreement.

Lee and Lu analyzed the free vibration of cylindrical shells in a liquid and a vacuum environment using Donnell's shell theory [30]. They modeled the internal fluid as inviscid and incompressible in order to use the velocity potential function, and resolved the hydrodynamic mass into a simplified approximation in the form of

$$M_H = \frac{\rho_f}{\rho_s}\frac{R}{h}\left(\lambda\frac{I_{n-1}(\lambda)}{I_n(\lambda)} - n\right)^{-1} \tag{5}$$

where I_n is the modified Bessel function of the first kind. The frequency equation was determined based on Galerkin's method [31] which offers significant economy in comparison to the 3x3 frequency matrix used in an alternative method [32]. Application of their simplified method yields the plot of Fig. 2 in which the frequency response of a cantilevered shell is shown for both a liquid-filled and vacuum environment.

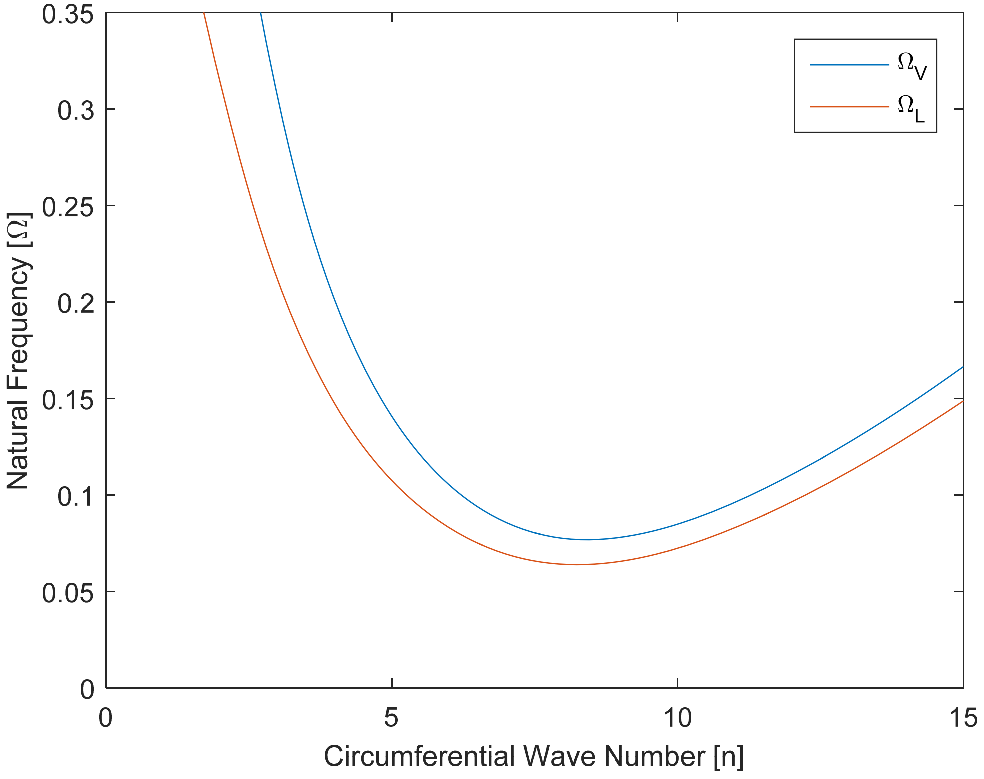

Fig. 2. Ω vs *n* for a shell in a fluid and in a vacuum

Two important observations are made from Fig. 2, the first being that the lowest frequency of the shell does not occur at the lowest circumferential wavenumber, however, it does occur at the lowest axial wavenumber [33]. The second observation is that the liquid-filled shell has a lower frequency than the shell in a vacuum; this is due to the fluid absorbing a fraction of the vibrations.

Chen and Rosenberg performed a large study on the dynamics of a two concentric cylindrical shells containing and separated by a fluid [34], extending the analysis performed by Païdoussis among others. Based on Flügge's shell equation [25], an exact derivation for the general frequency response of the coupled system was obtained in terms of a 9x9 coefficient matrix for the traveling wave solution. In addition to the exact frequency equation, they identified a simplified approximate solution for various specific cases by neglecting axial and tangential inertias and determined the frequency response for the in-phase and out-of-phase vibration modes of the shells. They made the observation that the lowest frequency of the coupled system is lower than that of the individual shells; the impact of this observation is that the behavior of two bodies coupled with a fluid could act as one entirely different system than the sum of its components. Other limiting cases were identified by calculating the dispersion relation ($n = 0$), the circumferential motions ($\alpha = 0$), and a rigid shell approximation ($h_j \gg 1$).

Krajcinovic performed a similar investigation as Chen in 1974 on the vibrations of two coaxial cylindrical shells of infinite length containing a flowing fluid [35]. In their study, they provided the justification for a few simplifying assumptions in regards to the hydrodynamic mass matrix. If the fluid velocity passing through the shells is small relative to the speed of sound in the medium, then the fluid may be considered to be incompressible. Additionally, the fluid flow in the axial direction may be neglected if the circumferential wavelength is small relative to the axial wavelength, which is usually satisfied in long slender cylinders. A numerical example was provided, comparing the results of the exact theory and the approximate theory, and it was shown that the differences were negligible in the frequency estimation, thus demonstrating that it is not necessary to use the exact solution if the two assumptions are valid.

Au-Yang performed an investigation similar to that of Krajcinovic, except extending the analysis to the free vibration of coaxial shells of finite lengths [36]. He identified the potential safety implications for coupling of lower axial modes via the relation

$$m_1 \approx m_2 \left(\frac{l_1}{l_2} \right). \tag{6}$$

For circumferential modes, coupling can only occur if the modes are the same for both shells ($n_1 = n_2$); for axial modes, however, coupling occurs when (6) is satisfied for $l_1/l_2 = 1, 1/2, 2/3, 3/4$, etc. Fig. 3 shows the in-phase and out-of-phase coupling for $l_1/l_2 = 1$ and $m = 1, 2, 3$.

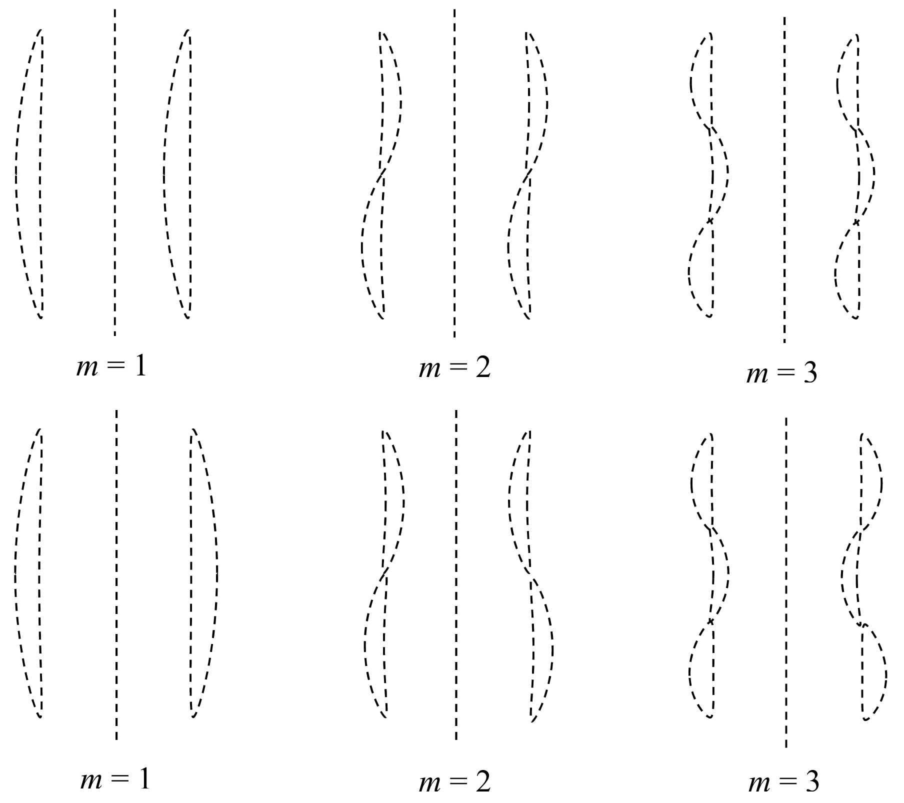

Fig. 3. In-phase (top) and out-of-phase (bottom) axial modes for concentric shells

In 1994, Naudascher and Rockwell published an engineering guide [37], compiling and summarizing a large body of work on the mechanisms of flow-induced vibration in common engineering applications. In this study, they discussed the works of several authors who had observed the 'ovalling', or circumferential mode, vibrations in cylindrical shells. Based on the dimensionless velocity proposed by Païdoussis and Helleur [38],

$$U_0 = U\left(\frac{\rho_s\left(1-\nu^2\right)}{E}\right)^{1/2}, \tag{6}$$

they compared multiple studies relating the shell thickness to the critical velocity in which the shell loses stability; this plot is presented in Fig. 4, and has been updated to include the prediction from the work of this study. The data of Fig. 4 [39, 40] implies an intuitive relation discussed in great length in this study; a thicker-walled shell requires a much higher flow velocity in order to undergo "flutter" or circumferential instability. It was noted in this reference that as the flow velocity (U) is increased, the natural frequency of the structure in fluid continually decreases until the critical point (U_{cr}) where the frequency goes to zero and the structure buckles in the first mode [41].

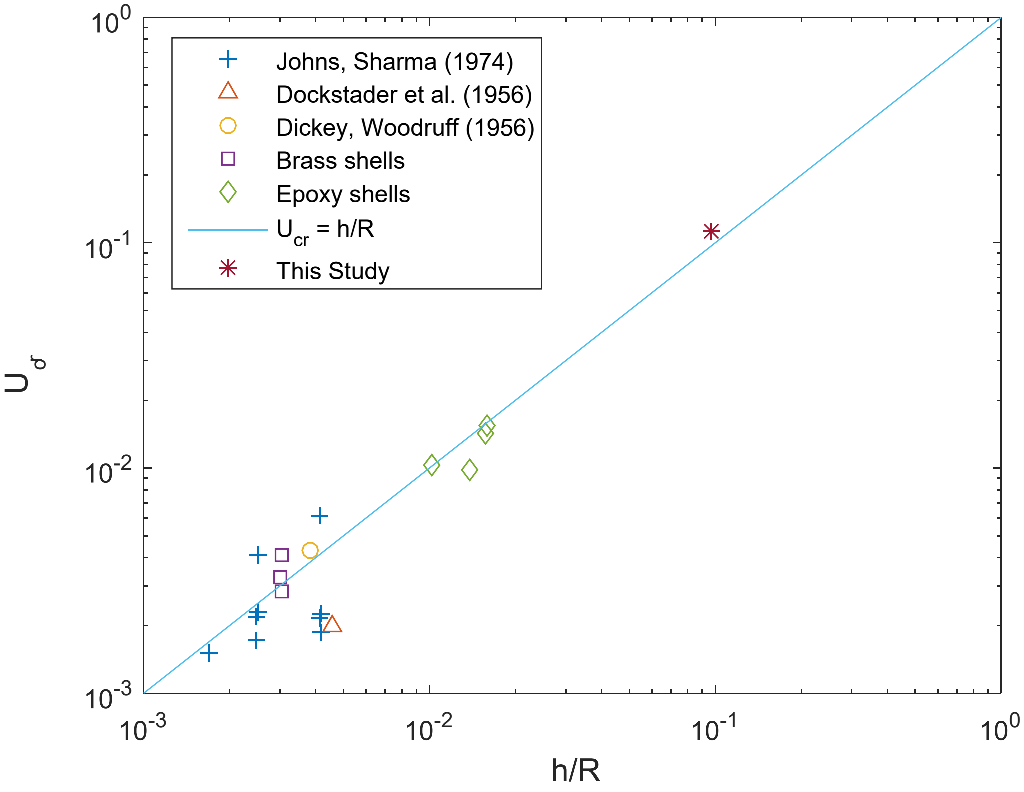

Fig. 4. Shell thickness-to-radius ratio vs buckling velocity

3 IN-PILE EXPERIMENT DESIGN

The experimental flow loop which was utilized to facilitate this experimental study was the Hydro-Mechanical Fuel Test Facility. The HMFTF is a large-scale hydraulic flow loop which has the capability to test a wide variety of full-scale fuel elements over a range of flow rates, temperatures, and pressures to match the thermal-hydraulic conditions of the various HPRRs. The facility, and the data generated from use of it is fully compliant with the American Society of Mechanical Engineers (ASME) NQA-1 2008, 2009a quality assurance standard. The flow is driven by either of the two primary centrifugal pumps on the facility, and the test element is placed inside of a test section of approximately 181 inches (4.6 meters) in height. Critical channels on the facility measure the state properties of the fluid in key locations which provide insight to the physics of the fluid-structure interaction. The facility may be modified to accommodate an up-flow or down-flow configuration inside the test section piping, and the physical response of the test element may be monitored via strain gauges, accelerometers, and pressure transducers.

As part of the National Nuclear Security Administration office of Material Management and Minimization, the Idaho National Laboratory is conducting a series of tests on prototypic fuel for the conversion of the five civilian high-performance research reactors in the US, and the HMFTF is aiding in these tests by performing out-of-pile flow testing prior to irradiation in the ATR. One such test, and the subject of this study, is the Miniplate-1 (MP-1) Large B (LB) test. The purpose of the MP-1 LB test is to benchmark the fabrication process and fuel performance of the monolithic Uranium-Molybdenum fuel selected for the conversion of these HPPRs [42]. In the context of this test, Miniplate refers to the scaled-down size of the fuel, which is to be irradiated in one of the four Large-B sample positions in the ATR. The pressure drop across the ATR is relatively fixed, thus it is desirable to confirm the computationally predicted flow rates through the experiment prior to its insertion into the core since it directly impacts the safety basis of the testing. Since this experiment is intended to quantify pressure drop and vibrational characteristics of the test element, a non-fueled mock-up hardware assembly was provided by the INL, thereby removing any unnecessary hazard associated with the handling and testing of radioactive material.

The MP-1 Large-B test hardware comprises the following elements, which are shown in Fig. 5 and Fig. 6 described as follows:

- **Miniplate Capsules**: Four capsules and three spacers are used for this test. The capsules are designated as capsules A, B, C, and D, and are stacked vertically in alphabetic order following the direction of flow. Two spacers are stacked on top of capsule A, and one spacer is below capsule D. The capsules comprise the core of the testing element, as they contain the mock fuel plates in a 2x4 configuration; two vertical rows of plates, with each row containing four equally spaced plates. Each miniplate capsule is approximately 8.38 inches (0.213 meters) in length, the bottom spacer is approximately 6.73 inches (0.171 meters) in length, the upper spacer is approximately 8.96 inches (0.228 meters) in length, and the top spacer is approximately 8.60 inches (0.218 meters) in length.

- **Vehicle**: The vehicle is the circular cylindrical housing in which all the miniplate capsules and spacers are stacked inside of. The vehicle is 2.5 inches (0.635 meters) in diameter and 60 inches (1.524 meters) in length and holds four capsules in series. The capsules slide inside the top of the vehicle and are guided by two rails on either side. The tolerances between the vehicle and the capsules are small enough such that, for the purposes of this test, they are considered to act as one body.
- **Flow Simulator:** The flow simulator is the cylindrical housing in which the test vehicle is seated inside of, providing a mechanical interface to the test element that is congruent with the geometries of the Large B experiment holder as seen within the ATR. The flow simulator also acts to secure the experiment to the test section within the HMFTF. Additionally, small plugs were placed in the flow paths within the flow simulator so that no flow could pass through the outside during testing.

Four accelerometers were secured to the experiment in different locations, in an attempt to capture the vibrational response of the element under the hydraulic loading. Accelerometers (Designated as Vibration Transmitters) VT-401 and VT-404 were secured to the vehicle bottom and top, respectively, and accelerometers VT-402 and VT-403 were secured to the flow simulator bottom and top, respectively, as shown in Fig. 6. The signal channels are designated as (a), (b), and (c), each corresponding to one of the Cartesian coordinates x, y, and z. The accelerometers are model 356M154/NC triaxial integrated circuit piezoelectric (ICP) accelerometers manufactured by PCB Piezotronics. They have a measurement range of ± 500g, a frequency range of 1 to 5000 Hz, and are a sealed design ideal for use in high-temperature fluid field applications.

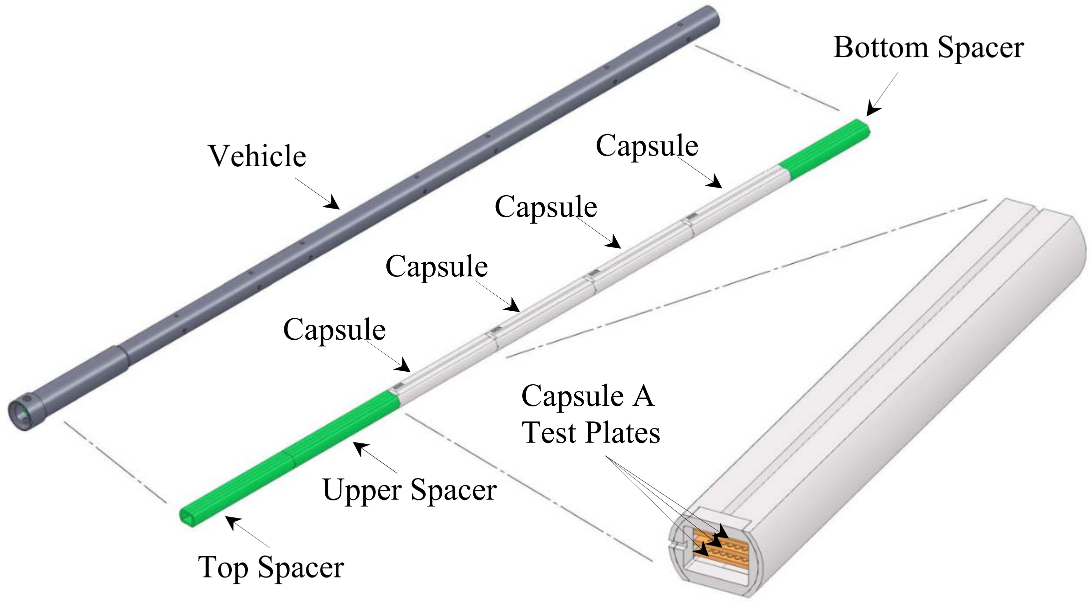

Fig. 5. Isometric view of experiment vehicle and capsules

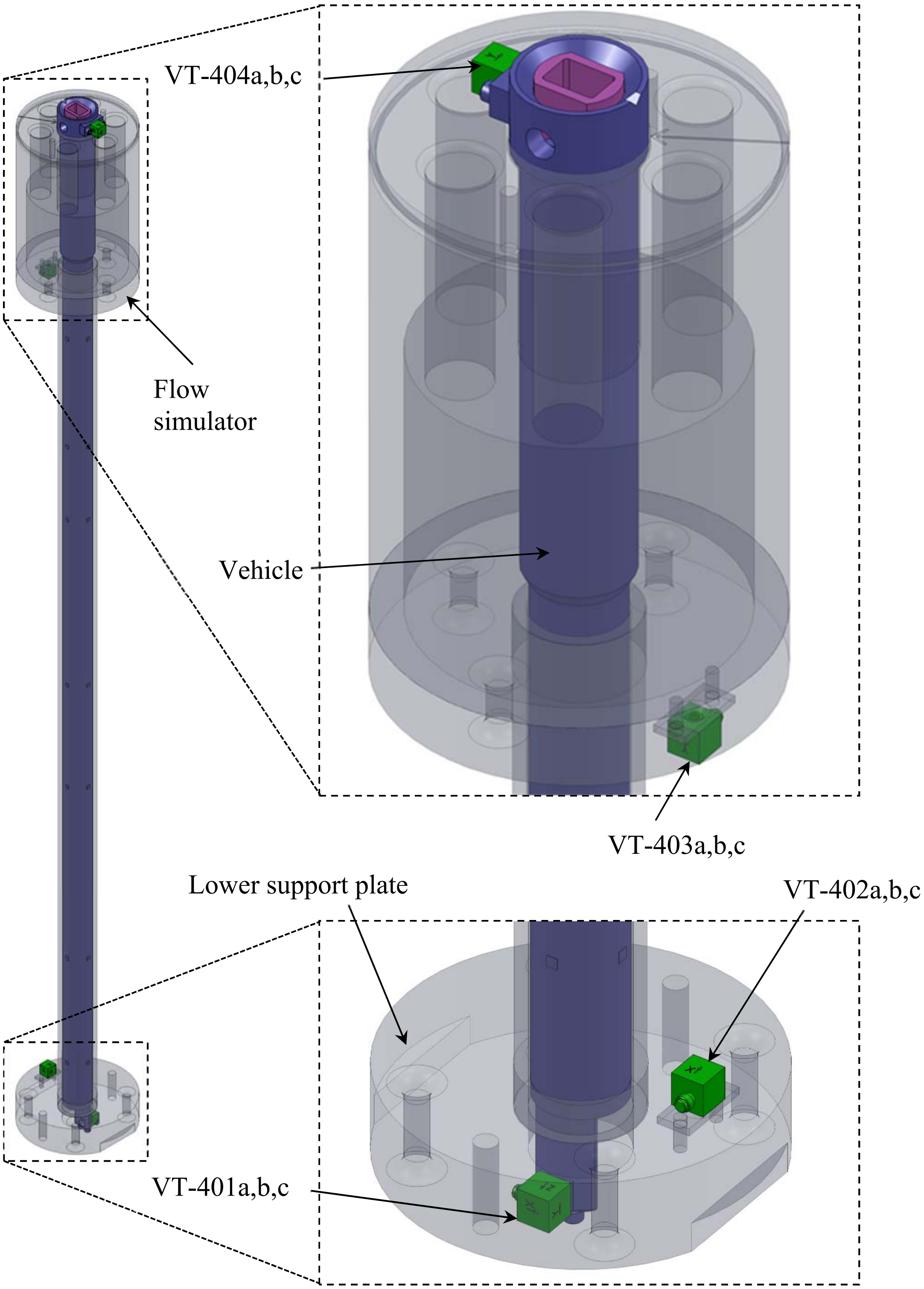

Fig. 6. Accelerometer mounting locations

The flow testing was carried out in a stepwise manner to characterize the response of the test element over a range of flow rates. The required initial and boundary conditions on the system during the test are shown in Table 1. Fluid pH and conductivity were controlled during the experiment; this was not necessarily influential of the immediate flow induced vibrational characteristics of the element, but rather impacts the oxidation rate of the aluminum hardware and therefore could impact the total mass and vibrational response in future experimental campaigns.

Table 1: Testing conditions

System Condition	Value	Units
Fluid pH	5.0 – 7.0	[#]
Fluid Conductivity	< 100	[μS/cm]
System Pressure	360 ± 5 (2.48 ± 0.03)	[psig] (MPa)
Fluid Temperature	150 ± 5 (65.55 ± 2.2)	[°F] (°C)
Initial Net Flow Rate	30 (1.89)	[gpm] (liters/s)
Final Pressure Drop	90 (0.621)	[psid] (MPa)

Once the initial system conditions were realized, the stair-step process could begin. The testing was conducted by holding steady at a given flow rate, beginning at 30 gpm, for a period greater than two minutes. At each flow rate, the software sampling rate was increased to 2000 Hz for a duration of 5 seconds, and then reduced back to the nominal sampling rate of 2 Hz. The flow rate was then increased by no more than 5 gpm, and the process was repeated until the final pressure drop of 90 psid was achieved as measured across the test element. The end of the test culminated in data collection for 15 different flow rate stair steps, tabulated in Table 2 [43].

Table 2: Stair step of flow rates and corresponding pressure drop during test

Stair Step [#]	Flow Rate [gpm] (liters/s)	Pressure Drop [psid] (MPa)
1	30.48 ± 1.45 (1.92 ± 0.09)	17.72 ± 0.90 (0.1222 ± 0.0062)
2	33.13 ± 1.45 (2.09 ± 0.09)	20.56 ± 0.90 (0.1418 ± 0.0062)
3	35.73 ± 1.40 (2.25 ± 0.09)	23.77 ± 0.90 (0.1639 ± 0.0062)
4	38.90 ± 1.48 (2.45 ± 0.09)	27.83 ± 0.90 (0.1919 ± 0.0062)
5	41.86 ± 1.53 (2.64 ± 0.10)	32.02 ± 0.91 (0.2208 ± 0.0063)
6	45.43 ± 1.63 (2.87 ± 0.10)	37.23 ± 0.91 (0.2567 ± 0.0063)
7	48.56 ± 1.63 (3.06 ± 0.10)	42.27 ± 0.91 (0.2914 ± 0.0063)
8	52.39 ± 1.73 (3.31 ± 0.11)	48.38 ± 0.90 (0.3336 ± 0.0062)

9	55.41 ± 1.75 (3.50 ± 0.11)	54.05 ± 0.90 (0.3727 ± 0.0062)
10	59.27 ± 1.80 (3.74 ± 0.11)	61.67 ± 0.90 (0.4252 ± 0.0062)
11	62.81 ± 1.91 (3.96 ± 0.12)	69.51 ± 0.90 (0.4793 ± 0.0062)
12	63.16 ± 1.83 (3.98 ± 0.12)	69.22 ± 0.90 (0.4773 ± 0.0062)
13	65.01 ± 1.90 (4.10 ± 0.12)	73.84 ± 1.09 (0.5091 ± 0.0075)
14	66.45 ± 1.97 (4.19 ± 0.12)	77.04 ± 0.92 (0.5312 ± 0.0063)
15	68.75 ± 1.94 (4.34 ± 0.12)	82.10 ± 1.07 (0.5661 ± 0.0074)
16	70.64 ± 2.02 (4.46 ± 0.13)	86.20 ± 0.90 (0.5943 ± 0.0062)
17	74.72 ± 2.02 (4.74 ± 0.13)	95.57 ± 0.90 (0.6589 ± 0.0062)

In addition to the test performed with the accelerometers, a separate flow test was performed which employed the use of a pitot tube array in an attempt to infer the flow rate of the coolant in each subchannel of the MP-1 capsules. In each subchannel, two pitot tubes were used: one to measure the static pressure, and one measure the dynamic pressure. From Bernoulli's principle, the fluid velocity can be calculated as

$$v = \left(\frac{2\Delta p}{\rho_f} \right)^{\frac{1}{2}} \tag{7}$$

where Δp is the pressure difference between the total and static pitot tubes, and ρ_f is the density of the fluid. Since the fluid temperature is constrained to a narrow bandwidth during testing, as shown in Table 1, then the density is assumed to remain constant throughout the test. The individual channel velocities have been calculated from (7) and are tabulated in Table 3 with all associated uncertainty and a level of 95 percent confidence.

Table 3: MP-1 capsule coolant channel velocities

Flow Rate [gpm] (liters/s)	Channel 1 Velocity [m/s]	Channel 2 Velocity [m/s]	Channel 3 Velocity [m/s]	Channel 4 Velocity [m/s]	Channel 5 Velocity [m/s]
30.29 ± 1.39 (1.91 ± 0.09)	6.93 ± 0.80	7.87 ± 0.71	8.44 ± 0.66	7.8 ± 0.71	6.66 ± 0.83
32.88 ± 1.39 (2.07 ± 0.09)	7.63 ± 0.73	8.58 ± 0.65	9.16 ± 0.61	8.58 ± 0.65	7.35 ± 0.76
36.12 ± 1.45 (2.28 ± 0.09)	8.36 ± 0.66	9.40 ± 0.59	9.91 ± 0.56	9.42 ± 0.59	8.12 ± 0.68
39.86 ± 1.57 (2.51 ± 0.10)	9.23 ± 0.60	10.46 ± 0.53	11.02 ± 0.50	10.5 ± 0.53	9.11 ± 0.61
43.81 ± 1.59 (2.76 ± 0.10)	10.32 ± 0.54	11.63 ± 0.48	12.16 ± 0.46	11.7 ± 0.47	10.19 ± 0.54
47.97 ± 1.63 (3.03 ± 0.10)	11.37 ± 0.49	12.82 ± 0.43	13.38 ± 0.41	12.95 ± 0.43	11.31 ± 0.49
52.50 ± 1.88 (3.31 ± 0.12)	12.57 ± 0.44	14.16 ± 0.39	14.72 ± 0.38	14.25 ± 0.39	12.49 ± 0.44
57.56 ± 1.79 (3.63 ± 0.11)	13.73 ± 0.40	15.56 ± 0.36	16.21 ± 0.34	15.71 ± 0.35	13.79 ± 0.40
63.12 ± 1.84 (3.98 ± 0.12)	15.19 ± 0.37	17.07 ± 0.33	17.76 ± 0.31	17.11 ± 0.32	15.06 ± 0.37
67.02 ± 2.24 (4.23 ± 0.14)	16.17 ± 0.34	18.24 ± 0.30	18.97 ± 0.29	18.22 ± 0.30	16.1 ± 0.34

For the purpose of analytically determining the dynamic response of the test element in a later part of this study, it is desirable to know both the internal flow velocity through the plates, and the external flow velocity which passes around the experiment vehicle. The total flow, Q_t, is measured from the system's vortex flow meter, and the flow through the inside of the vehicle, Q_i, can be inferred from (7) and the geometry of the coolant channels. Thus the external flow can be calculated as

$$Q_e = Q_t - \sum_{i=1}^{5} v_i A_i , \tag{8}$$

where v_i is the flow velocity from (7) and A_i is the cross-sectional area of the coolant channel.

The result of (8) with the sum of a the total effective uncertainty using 95 percent confidence on the stochastic variance shows that the uncertainty is too high to confidently infer the quantity, if any, of flow passing through the annulus between the experiment vehicle and the flow simulator. Thus the internal flow is taken as the total flow, as measured by the system's vortex flowmeter.

Fig. 7 shows the results of the testing for each triaxial accelerometer for a specific flow rate. The output is in units of gravity and the relative magnitudes of acceleration can be inferred at each point on the experiment. It is from this data that the motion of the test section can be analyzed to understand its dynamic behavior in the flow field. In all plot traces within figure 7, the *x*-axis, representing sample time is taken over 5 seconds; the *y*-axis reflecting acceleration in g's is bound from -1.5 to 1.5 in all subplots.

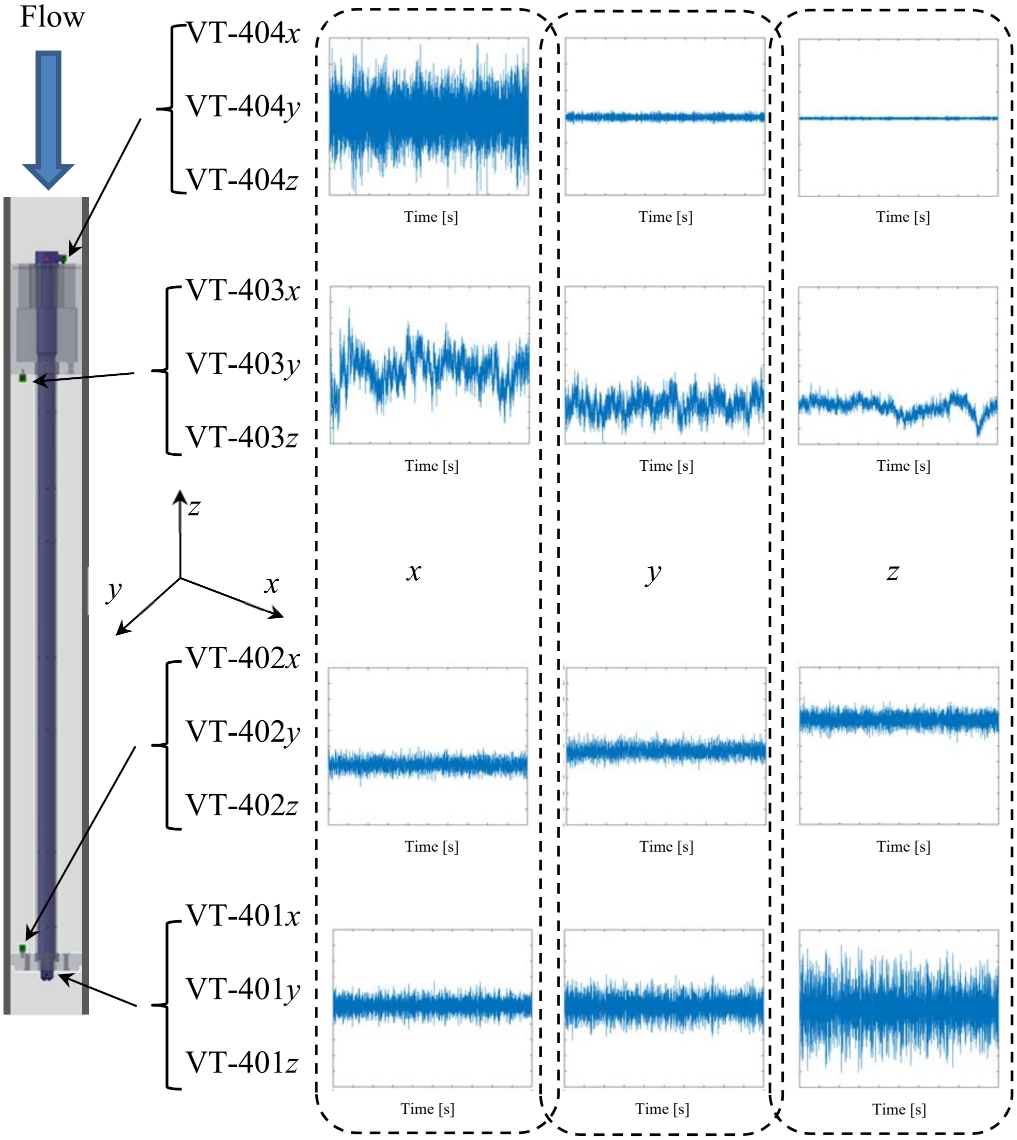

Fig. 7. Triaxial accelerometer output for one flow rate

4 SEMINUMERICAL MODELS

The formulation of a vibration model begins with making some simplifying assumptions in regards to the geometry and the physics of the problem. The underlying model is assumed to consist of two coaxial cylindrical shells conveying an inviscid fluid; the displacement of this system is determined from Flügge's shell equations [25]:

$$\begin{aligned}&\left(\frac{\partial^2}{\partial z^2}+\left(\frac{1-\nu_j}{2R_j^2}\right)\left(1+\frac{h_j^2}{12R_j^2}\right)\frac{\partial^2}{\partial\theta^2}\right)\alpha_j+\left(\frac{1+\nu_j}{2R_j}\right)\frac{\partial^2\beta_j}{\partial z\,\partial\theta}\\&\qquad+\left(\frac{\nu_j}{R_j}\frac{\partial}{\partial z}-\frac{h_j^2}{12R_j}\frac{\partial^3}{\partial z^3}+\frac{\left(1-\nu_j\right)h_j^2}{24R_j^{\,3}}\frac{\partial^3}{\partial z\,\partial\theta^2}\right)\gamma_j=\frac{\rho_{sj}\left(1-\nu_j^2\right)}{E_j}\frac{\partial^2\alpha_j}{\partial t^2},\end{aligned}\tag{9}$$

$$\begin{aligned}&\left(\frac{1+\nu_j}{2R_j}\frac{\partial^2}{\partial z\,\partial\theta}\right)\alpha_j+\left(\frac{1}{R_j^2}\frac{\partial^2}{\partial\theta^2}+\frac{1-\nu_j}{2}\left(1+\frac{h_j^2}{4R_j^2}\right)\frac{\partial^2}{\partial z^2}\right)\beta_j\\&\qquad+\left(\frac{1}{R_j^2}\frac{\partial}{\partial\theta}-\frac{\left(3-\nu_j\right)h_j^2}{24R_j^2}\frac{\partial^3}{\partial\theta\,\partial z^2}\right)\gamma_j=\frac{\rho_{sj}\left(1-\nu_j^2\right)}{E_j}\frac{\partial^2\beta_j}{\partial t^2},\end{aligned}\tag{10}$$

and

$$\begin{aligned}&\left(-\frac{h_j^2}{12R_j}\frac{\partial^3}{\partial z^3}+\frac{\nu_j}{R_j}\frac{\partial}{\partial z}+\frac{\left(1-\nu_j\right)h_j^2}{24R_j^3}\frac{\partial^3}{\partial z\,\partial\theta^2}\right)\alpha_j\\&\qquad+\left(-\frac{\left(3-\nu_j\right)h_j^2}{24R_j^2}\frac{\partial^3}{\partial\theta\partial z^2}+\frac{1}{R_j^2}\frac{\partial}{\partial\theta}\right)\beta_j\\&\qquad\qquad+\begin{pmatrix}\dfrac{1}{R_j^2}+\dfrac{h_j^2}{12R_j^4}+\dfrac{h_j^2}{12}\dfrac{\partial^4}{\partial z^4}+\dfrac{h_j^2}{6R_j^2}\dfrac{\partial^4}{\partial z^2\partial\theta^2}\\+\dfrac{h_j^2}{12R_j^4}\dfrac{\partial^4}{\partial\theta^4}+\dfrac{h_j^2}{6R_j^4}\dfrac{\partial^2}{\partial\theta^2}\end{pmatrix}\gamma_j\\&\qquad\qquad+\frac{\rho_{sj}\left(1-\nu_j^2\right)}{E_j}\frac{\partial^2\gamma_j}{\partial t^2}=\frac{\left(1-\nu_j^2\right)}{E_jh_j}p_j\end{aligned}\tag{11}$$

In (9) through (11), the subscript j is used to denote the inner (j = 1) and outer (j = 2) shells. The midpoint axial, tangential, and radial displacements are denoted by $\alpha_j(r, \theta, z)$, $\beta_j(r, \theta, z)$, and $\gamma_j(r, \theta, z)$, respectively, and p_j is the hydrodynamic pressure. The physical parameters associated with the experiment which are to be used as inputs in the system of equations are tabulated in Table 4, where the inner shell is analogous to the capsule vehicle, and the outer shell is analogous to the flow simulator.

Table 4: Physical parameters associated with shells

Parameter	Inner Shell (*j* = *1*)	Outer Shell (*j* = *2*)
Inner radius, R_j, [m]	0.016675	0.01905
Length, L_j, [m]	1.50495	1.50495
Wall Thickness, h_j [m]	0.0016	0.0051
Structural Density, ρ_j [kg/m^3]	2.7 x 10^3	2.7 x 10^3
Young's modulus, E_j, [Pa]	69 x 10^9	69 x 10^9
Poisson's Ratio, v_j [#]	0.35	0.35

The solution proceeds in the same manner as discussed in similar studies on the dynamic response of circular cylindrical shells conveying fluid [18, 35, 44]. That is, the solution to (9) through (11) will be in the form of a traveling wave with complex coefficients, and is dependent on not only the physical parameters defined in Table 4, but also of both the circumferential and axial wave numbers [32]. The fluid is also to be treated as a potential flow and satisfies Laplace's equation. The assumed solution form of the displacement of the shell is given as

$$\alpha_j = \mathrm{A}_j \exp\left(i\left(\frac{\lambda_j x}{R_j} + n\theta_j + \omega_j t\right)\right) \tag{12}$$

$$\beta_j = \mathrm{B}_j \exp\left(i\left(\frac{\lambda_j x}{R_j} + n\theta_j + \omega_j t\right)\right) \tag{13}$$

$$\gamma_j = \Gamma_j \exp\left(i\left(\frac{\lambda_j x}{R_j} + n\theta_j + \omega_j t\right)\right) \tag{14}$$

where A_j, B_j, and Γ_j are the complex coefficients, *i* is the imaginary unit, λ_j is the axial wavenumber, R_j is the shell inner-radius, *n* is the circumferential mode, ω is the circular frequency, and *t* is the time. Then (13) through (14) are substituted into (9) through (11) resulting in the 6x6 matrix [18]

$$\begin{bmatrix} C_{11} & C_{12} & C_{13} & 0 & 0 & 0 \\ C_{21} & C_{22} & C_{23} & 0 & 0 & 0 \\ C_{31} & C_{32} & C_{33} & 0 & 0 & C_{36} \\ 0 & 0 & 0 & C_{44} & C_{45} & C_{46} \\ 0 & 0 & 0 & C_{54} & C_{55} & C_{56} \\ 0 & 0 & C_{63} & C_{64} & C_{65} & C_{66} \end{bmatrix} \begin{bmatrix} \mathrm{A}_1 \\ \mathrm{B}_1 \\ \Gamma_1 \\ \mathrm{A}_2 \\ \mathrm{B}_2 \\ \Gamma_2 \end{bmatrix} = \begin{bmatrix} 0 \\ 0 \\ 0 \\ 0 \\ 0 \\ 0 \end{bmatrix}. \tag{15}$$

In (15) each coefficient (C_{ij}) is defined, respectively as

$$C_{11} = C_{44} = -\lambda_j^{\,2} - \left(\frac{1-\nu_j}{2}\right) n^2 \left(1+\kappa_j\right) + \Omega_j^{\,2} \,, \tag{16}$$

$$C_{12} = C_{45} = -i\left(\frac{1-\nu_j}{2}\right)\lambda_j n \,, \tag{17}$$

$$C_{13} = C_{46} = -i\left(\lambda_j \nu_j + \kappa_j\left(\lambda_j^{\,3} - \left(\frac{1-\nu_j}{2}\right)\lambda_j n^2\right)\right), \tag{18}$$

$$C_{21} = C_{54} = -i\left(\frac{1-\nu_j}{2}\right)\lambda_j n \,, \tag{19}$$

$$C_{22} = C_{55} = n^2 + \left(\frac{1-\nu_j}{2}\right)\left(1+3\kappa_j\right)\lambda_j^{\,2} - \Omega_j^2 \,, \tag{20}$$

$$C_{23} = C_{56} = n^2 + \kappa_j\left(3-\nu_j\right) n \lambda_j^2 \,, \tag{21}$$

$$C_{31} = C_{64} = -i\left(\lambda_j \nu_j + \kappa_j\left(\lambda_j^{\,3} - \left(\frac{1-\nu_j}{2}\right)\lambda_j n^2\right)\right), \tag{22}$$

$$C_{32} = C_{65} = n^2 + \kappa_j\left(3-\nu_j\right) n \lambda_j^2 \,, \tag{23}$$

$$C_{33} = C_{66} = 1 + \kappa_j\left(\left(\lambda_j^{\,2} + n^2\right)^2 - 2n^2 + 1\right) - \Omega_j^{\,2} - \mu_j C_{m1}\left(\Omega_j + \overline{U}_j \lambda_j\right)^2 , \tag{24}$$

and

$$C_{36} = C_{63} = \mu_j C_{m2} \Omega_j^{\,2} \,. \tag{25}$$

These coefficients are driven by the variables

$$\kappa_j = \frac{\delta_j^{\,2}}{12} \,, \tag{26}$$

$$\delta_j = \frac{h_j}{R_j} \,, \tag{27}$$

$$\mu_j = \frac{\rho_f}{\delta_j \rho_j} \,, \tag{28}$$

$$\Omega_j = R_j \omega_j \left(\frac{\rho_j\left(1-\nu_j^{\,2}\right)}{E_j}\right)^{1/2} , \tag{29}$$

$$\omega_j = 2\pi f_j \,, \tag{30}$$

and

$$\overline{U}_j = U_j \left(\frac{\rho_j \left(1 - \nu_j^{\ 2}\right)}{E_j} \right)^{1/2}, \tag{31}$$

where h_j is the shell thickness, ρ_f is the fluid density, ρ_j is the shell density, ν_j is Poisson's ratio, E_j is Young's modulus, f_j is the ordinary frequency, U_j is the superficial fluid velocity, and C_m is the coefficient of hydrodynamic mass. The superficial velocity detailed throughout this study reflects ratio of the volume flow rate to cross sectional flow area within the capsule. As discussed in a number of other studies [18, 30, 35], the hydrodynamic mass coefficient is a cumbersome calculation in terms of the unknown dimensionless frequency, Ω, and is very sensitive to the axial (m) and circumferential (n) mode. Chen calculated the values of C_m out for a number of different geometries [21]; for the case of this study where the ratio of R_2 to R_1 is approximately 1.1, the values are presented below in Fig. 8.

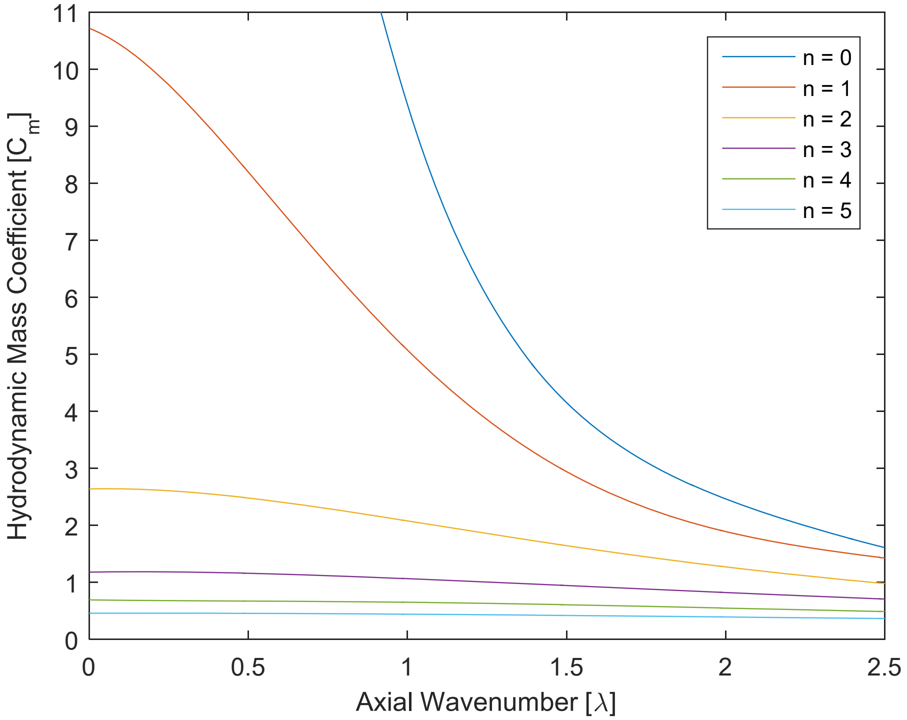

Fig. 8. Values of C_{m1} vs λ for different values of n with $R_2/R_1 = 1.1$

It can be seen from this plot that the values of C_m quickly approach some asymptotic value as both λ and n get large. Furthermore, it was noted that the following simple analytic approximation can be made for C_m where

$$C_{m1} \cong \frac{1}{n}\left(\frac{1+\left(R_1/R_2\right)^{2n}}{1-\left(R_1/R_2\right)^{2n}}\right), \tag{32}$$

and

$$C_{m2} \cong -\frac{2}{n}\frac{\left(R_1/R_2\right)^{n-1}}{1-\left(R_1/R_2\right)^{2n}}. \tag{33}$$

These two approximations are valid under two assumptions: (1) the fluid is incompressible, and (2) the axial fluid flow has a negligible effect on the structural vibrations [44]. The first assumption is validated by calculating the Mach number of the flow which is defined herein as

$$\mathrm{Ma} \equiv \frac{U_{\max}}{c} \tag{33}$$

To maintain conservatism, the highest flow velocity through the fuel plates is chosen as the flow velocity ($U_{\max} = 21.12$ m/s). The speed of sound in water (c) at 150 F is approximately 5100 m/s, from which the Mach number may then be tabulated through use of (33) to be 0.004. Since Ma = 0.004 ≪ 1, then the assumption of incompressibility is shown to be valid for this case. To consider the second case, the fluid velocity is non-dimensionalized in terms of (31) and the values defined in Table 4. This also results in a fluid velocity ($\overline{U}_{\max}$) of 0.004. Again, since $\overline{U}_{\max} = 0.004 \ll 1$, then the axial flow of fluid can be neglected and relations (32) and (33) are shown to be valid for this case.

Returning to (15), it is seen that the determinant of the coefficient matrix yields the frequency response function of the coupled shell-fluid system. In addition to the assumptions of compressibility and axial flow, further insight to the problem can greatly simplify the matrix to yield specific cases of interest. For slender cylindrical shells, the axial and tangential inertias are negligible with respect to the radial inertia ($A_j = B_j = 0$) [18]. Under this assumption, (15) reduces to

$$\begin{bmatrix} \Omega_{V1}^2 - C_1\Omega_1^2 & C_2\Omega_1^2 \\ C_3\Omega_1^2 & \Omega_{V2}^2 - C_4\Omega_1^2 \end{bmatrix} \begin{bmatrix} \Gamma_1 \\ \Gamma_2 \end{bmatrix} = \begin{bmatrix} 0 \\ 0 \end{bmatrix} \tag{34}$$

where Ω_{V1} and Ω_{V2} are the frequency equations for each shell in a vacuum given by

$$\Omega_{Vj} = \left(\kappa_j \left(\lambda_j^2 + n^2 \right)^2 + \frac{\left(1 - \nu_j^2\right)\lambda_j^4}{\left(\lambda_j^2 + n^2\right)^2} \right)^{1/2} \tag{35}$$

and the coefficients C_1 through C_4 are defined as

$$C_1 = 1 + \mu_1 C_{m1}, \tag{36}$$

$$C_2 = \mu_1 C_{m2}, \tag{37}$$

$$C_3 = \mu_2 C_{m2} R_{12}^2, \tag{38}$$

$$C_4 = \left(1 + \mu_2 C_{m1}\right) R_{12}^2, \tag{39}$$

and

$$R_{12} = \frac{R_2}{R_1}. \tag{40}$$

The values of κ_j, δ_j, and μ_j are calculated from Table 4 and are tabulated below:

Table 5: Values of δ_j, μ_j, and κ_j

Parameter	Inner Shell (*j = 1*)	Outer Shell (*j = 2*)
δ_j	0.096	0.268
μ_j	3.77	1.35
κ_j	7.7×10^{-4}	59.8×10^{-4}

From (34), six scenarios are examined: the frequency response of the coupled shell-fluid system (1) with a rigid outer-shell, (2) with a rigid inner-shell, (3) in their out-of-phase mode, (4) in their in-phase mode, (5) with the inner-shell in a vacuum, and (6) with the outer-shell in a vacuum. Cases (1) and (2) are analyzed by making the wall thickness become very large ($h_j \rightarrow \infty$), forcing μ_j to go to zero. Cases (3) and (4) are analyzed by taking the determinant of (34) and solving for the two frequency components. Cases (5) and (6) are analyzed by solving (35) and setting ρ_f equal to zero. The equations for all six cases are summarized below.

$$\Omega_1 = \left(\frac{\Omega_{V1}^2}{C_1} \right)^{1/2} \tag{41}$$

$$\Omega_1 = \left(\frac{\Omega_{V2}^2}{C_4} \right)^{1/2} \tag{42}$$

$$\det \begin{vmatrix} \Omega_{V1}^2 - C_1\Omega_1^2 & C_2\Omega_1^2 \\ C_3\Omega_1^2 & \Omega_{V2}^2 - C_4\Omega_1^2 \end{vmatrix} = 0 \tag{43}$$

$$\Omega_{V1} = \left(\kappa_1 \left(\lambda_1^2 + n^2 \right)^2 + \frac{\left(1-\nu_1^2\right)\lambda_1^4}{\left(\lambda_1^2 + n^2\right)^2} \right)^{1/2} \tag{44}$$

$$\Omega_{V2} = \left(\kappa_2 \left(\lambda_2^2 + n^2 \right)^2 + \frac{\left(1-\nu_2^2\right)\lambda_2^4}{\left(\lambda_2^2 + n^2\right)^2} \right)^{1/2} \tag{45}$$

The equations above are physically analogous to a rigid outer-shell (41), a rigid inner-shell (42), the in-phase and out-of-phase modes (43), the inner-shell in a vacuum (44), and the outer-shell in a vacuum (45) [18].

It can be seen from (41) through (45) that the additional fluid loading results in a decrease in natural frequency. Applying these equations to the geometry of this system results in the plots of Fig. 9.

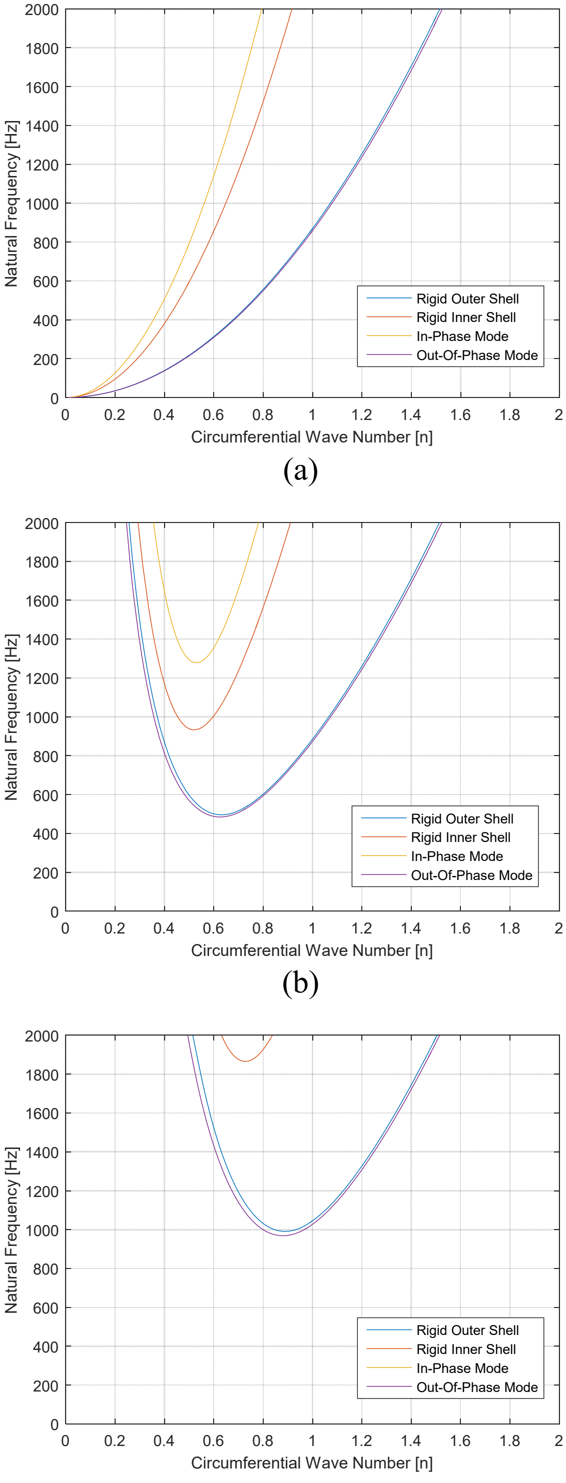

(a)

(b)

(c)

Fig. 9. Frequency plot for coaxial shells in fluid for (a) $m = 0$, (b) $m = 1$, and (c) $m = 2$

Fig. 9 presents the frequency response as a function of circumferential wave number, n, for the first three axial modes, $m = 0$, 1, and 2. As expected, the natural frequency of each the coupled fluid-shell system increases with a corresponding increase in axial vibration mode. Furthermore it can be seen that the lowest frequency does not correspond to the lowest circumferential wave number, which is unique to the cylindrical shells. The lower-frequency vibrations are predicted to occur in the out-of-phase mode of the coaxial shells, and the frequency spectrum in each case is nearly identical to that of the rigid outer-cylinder assumption.

The case of $m = 0$ is trivial by nature and the case of $m = 2$ nearly exceeds the Nyquist frequency captured by the accelerometers, so the case of $m = 1$ is analyzed for comparison. It is seen that the lowest fundamental frequency occurs for the rigid outer-shell assumption and the out-of-phase modes at approximately 500 Hz, for the rigid inner-shell approximation at approximately 975 Hz, and in the in-phase mode at approximately 1300 Hz. It is also interesting to see that the rigid outer-shell and out-of-phase modes occur at the same value of n, while the inner-shell and in-phase modes occur at the same value of n.

These results are consistent with intuition of the physical system in that the shells are relatively thick-walled ($h/R \approx 0.1$), thus the solution should not show the fundamental frequency to be of the higher circumferential modes (i.e. $n = 2, 3, 4$, etc.). This is seen in the plots above where, for the first three axial modes, the fundamental frequency does not occur higher than the first circumferential mode ($n = 1$). Thus it could be said that the physical system may be approximated as two coaxial thick-walled pipes and the calculation of the frequency response of this system can be simplified in terms of just the beam equations.

5 EXPERIMENTAL ANALYSIS

The culmination of testing requires a statistical analysis on the spectral response of the test element to determine which peaks are significant relative to the others. Furthermore, a significant number of accelerometer signals are either entirely unusable, or the signal was lost at some point during testing; this is due to either damage to the cable, or the accelerometer itself. The table below outlines which signals can be used for the purpose of the final analysis, and which cannot.

Table 6: Accelerometer signal used [✓] and not-used [✗]

VT	Stair Step Number																
	01	02	03	04	05	06	07	08	09	10	11	12	13	14	15	16	17
401x	✓	✓	✓	✓	✓	✓	✓	✓	✓	✓	✓	✓	✓	✓	✓	✓	✓
401y	✓	✓	✓	✓	✓	✓	✓	✓	✓	✓	✓	✓	✓	✓	✓	✓	✓
401z	✓	✓	✓	✓	✓	✓	✓	✓	✓	✓	✓	✓	✓	✓	✓	✓	✓
402x	✓	✓	✓	✓	✓	✓	✓	✓	✓	✓	✓	✓	✓	✓	✓	✓	✓
402y	✓	✓	✓	✓	✓	✓	✓	✓	✓	✓	✓	✓	✓	✓	✓	✓	✓
402z	✓	✓	✓	✓	✓	✓	✓	✓	✓	✓	✓	✓	✓	✓	✓	✓	✓
403x	✗*	✗*	✗*	✗*	✗*	✗*	✗*	✗*	✗*	✗*	✗*	✗*	✗*	✗*	✗*	✗*	✗*
403y	✗*	✗*	✗*	✗*	✗*	✗*	✗*	✗*	✗*	✗*	✗*	✗*	✗*	✗*	✗*	✗*	✗*
403z	✗*	✗*	✗*	✗*	✗*	✗*	✗*	✗*	✗*	✗*	✗*	✗*	✗*	✗*	✗*	✗*	✗*
404x	✓	✓	✓	✓	✓	✓	✗	✗	✗	✗	✗	✗	✗	✗	✗	✗	✗
404y	✓	✗	✗	✗	✗	✗	✗	✗	✗	✗	✗	✗	✗	✗	✗	✗	✗
404z	✓	✓	✓	✓	✓	✗	✗	✗	✗	✗	✗	✗	✗	✗	✗	✗	✗

From Table 6, it can be seen that VT-401 and VT-402 provide a usable response across the entire range of testing, while VT-403 and VT-404 do not. The asterisk on VT-403 [✗*] is used to denote the fact that while the signal-to-noise ratio is too low to integrate the data to yield the displacement, there are a few noticeable frequency peaks which can be seen, the most prevalent being a spike at the 60 Hz frequency. This is a result of the vibration of the centrifugal pump being used to drive the flow for the test; since the electrical utilities operate on a three-phase 60 Hz cycle, this peak is expected. An example of the frequency spectra for each accelerometer is shown below at stair step number three (corresponding to 35.7 gpm).

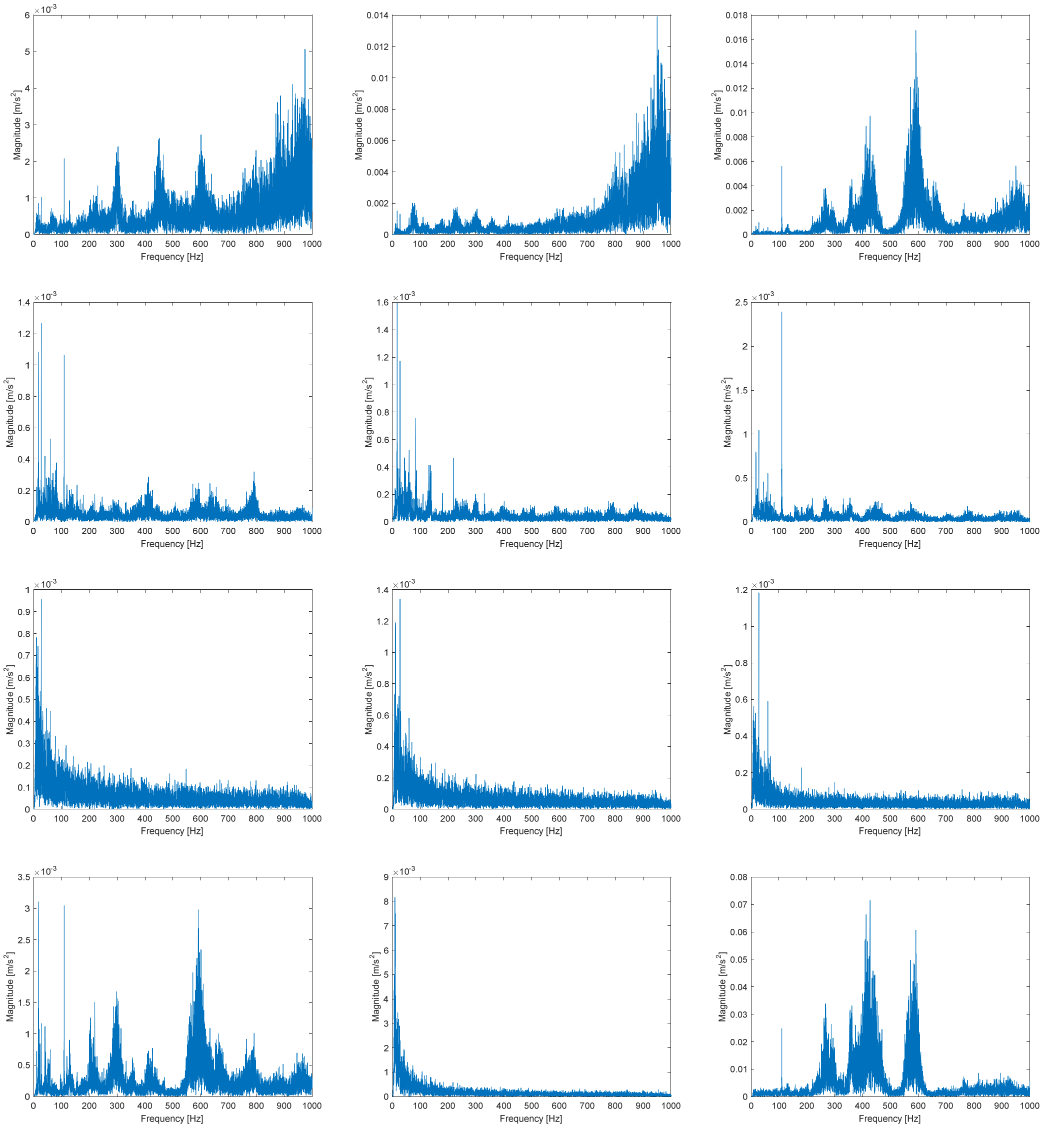

Fig. 10. (x, y, z) frequency response of each accelerometer at 35.7 gpm

In Fig. 10, the frequency response can be seen from VT-401 (top row), VT-402 (second row), VT-403 (third row), and VT-404 (bottom row); the x, y, and z response of each VT is shown from left to right, respectively. The x-axis and y-axis in each plot within Fig. 10 represent frequency Hz and magnitude in m/s^2, respectively. The location and direction of these accelerometer readings is physically located on the vehicle as shown in Fig. 6. Statistically significant peaks are determined according to the following criteria:

$$peak = \frac{1}{N}\sum_{i=1}^{N} a_{FFT} + (2\sigma), \tag{46}$$

where σ is the standard deviation of the frequency plot. Unfortunately, the repeatability and reliability of this approach changes depending on the accelerometer behavior. For example, (46) is applied to VT-401x and is shown below in Fig. 11.

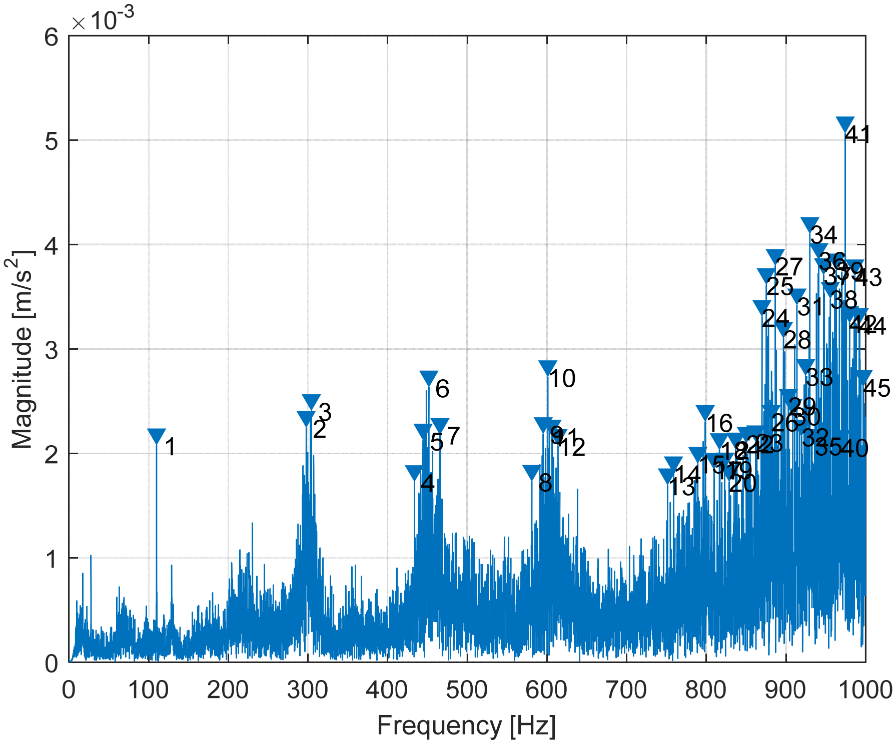

Fig. 11. VT-401x at 35.7 gpm with peaks two standard deviations from signal mean, with high-frequency Gaussian white noise

It can be seen that there is one sharp peak that occurs at 110 Hz, and then the following three more broad peaks occur at approximately 300, 450, and 600 Hz. At frequencies higher than about 750 Hz, however, it can be seen that although there are many frequencies that meet the criteria, there is no real coherent peak. This is characteristic of the Gaussian white noise which is commonly seen in higher frequencies of accelerometers [45]; it will be demonstrated shortly that this noise is reduced through the double-integration process. Another phenomena seen in the accelerometer signals from this test is that of the $1/f$ noise which occurs at low frequencies, shown below in Fig. 12.

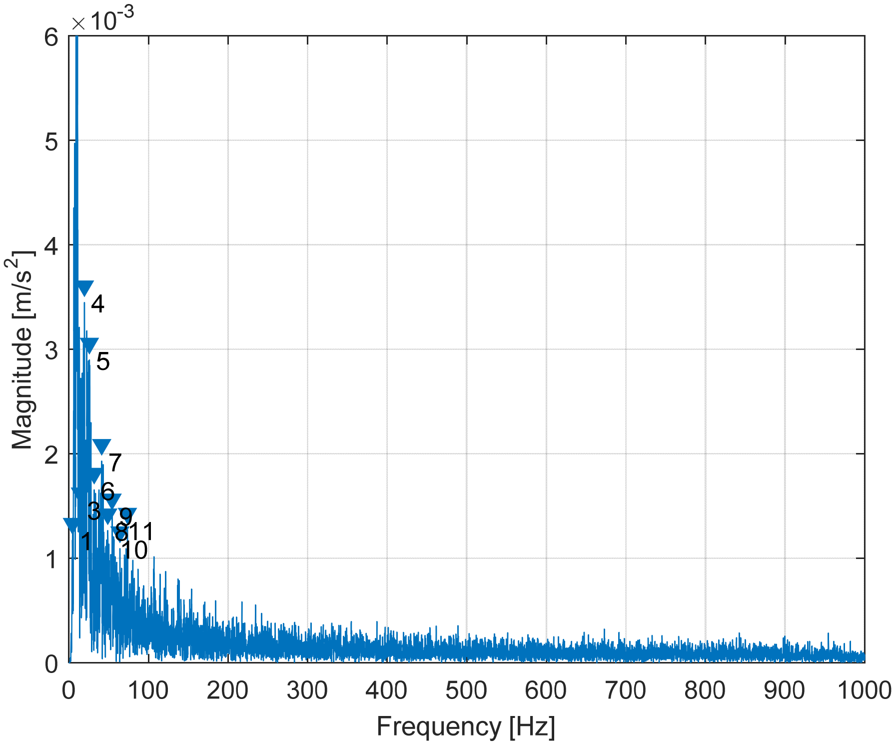

Fig. 12. VT-404y at 35.7 gpm with peaks two standard deviations from signal mean, with low-frequency 1/*f* noise

This is noise is characterized by the spectral plot magnitude decreasing from the 0 Hz range approximately proportional to 1/*f*; this behavior is seen not only in accelerometer signals, but across many disciplines. Unlike the higher-frequency Gaussian white noise, it cannot be simply attenuated by the integration process nor can it be mitigated through the use of a digital filter.

The frequency response of the test element can be better understood by viewing the waterfall plot of each accelerometer’s spectral response as a function of the total system flow rate, for example the plot of Fig. 13.

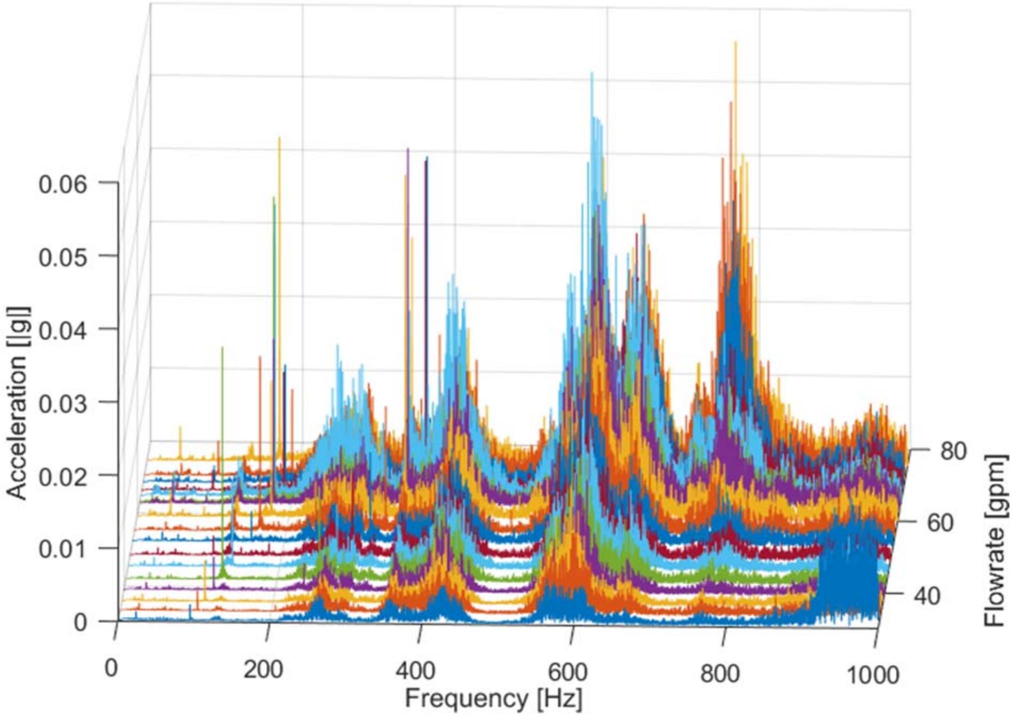

Fig. 13. Waterfall plot of VT-401y

From this plot, the frequency peaks can be categorized into one of two types: structural and hydrodynamic [46]. The structural frequencies are characterized by the large, broad peaks which remain constant with flow rate; this was predicted through the vibration model analysis in the previous section which showed the relatively low impact the flow velocity has on the natural frequency of the cylindrical structure. The second category is that of the hydrodynamic peaks, which are characterized by the sharp, singular peaks, and they can be seen to increase proportional to the flow rate. The origin of these hydrodynamic frequencies are from the vortices shed off the internal structure of the test element, most prominently from the plates in the MP-1 capsules. These frequencies can be characterized in terms of the Strouhal number of (1) where f is the frequency observed in the spectral plots vs flow rate, D is the associated length or hydraulic diameter, and U is the superficial flow velocity. It is evident from Fig. 13 that there are multiple sets of these hydrodynamic modes which occur simultaneously at different frequencies; for VT-401, there are three well-defined frequency modes and they have been tabulated and are plotted versus U below in Fig. 14(a). For VT-402, the same hydrodynamic frequency modes as those in VT-401 were identified, in addition to one higher mode, as shown below in Fig. 14 (b).

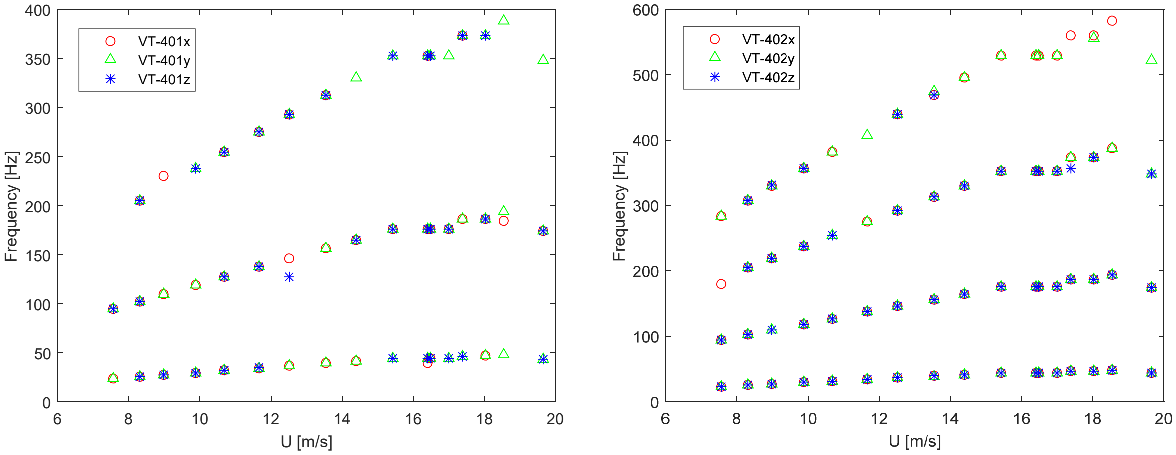

(a) (b)

Fig. 14. Hydrodynamic frequency vs *U* for (a) VT-401 and (b) VT-402

It can be seen from these plots that as the flow velocity is increased, the frequency increases by a linearly proportional amount until lock-in is achieved briefly at approximately the 16 m/s mark, after which the frequency continues to increase. When each frequency set is correlated to the chord length of the plates and the flow velocity, it can be seen that each of the hydrodynamic modes correspond to a specific Strouhal number, as shown in Fig. 15.

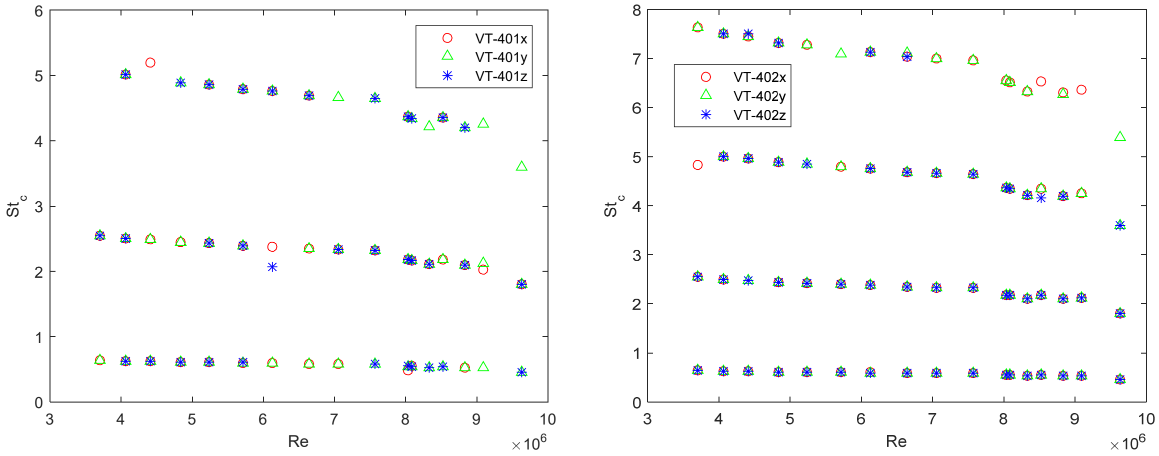

(a) (b)

Fig. 15. Hydrodynamic peak Strouhal- vs Reynolds-number in (a) VT-401 and (b) VT-402

For the lower modes of vibration, it can be seen that the resulting Strouhal number is relatively constant, while the higher frequency modes drop of slightly with a corresponding increase in the Reynolds number. Note that the Strouhal number in Fig. 15 is defined in terms of the chord length of the plate, St_C, but in some works of literature the author chooses to represent it in terms of the plate thickness, St_t, as well [47].

Employing the use of (46), the waterfall plot of Fig. 13 can be represented in a 2-dimensional fashion similar to Fig. 14 to display only the statistically significant peaks and identify the large magnitude structural vibrations as a function of flow rate. In Fig. 16, it can be seen that in the *x*-direction in the lower flow rates, there are four significant peaks four in both accelerometers. As flow rate is increased, the lower-frequency hydrodynamic peaks are seen to increase, while the broader structural peaks remain relatively constant in the 300-700 Hz range. In the *y*-direction, the same trend is observed to be consistent, with the lower-frequency peaks increasing with flow rate and three clear structural peaks observed in the higher-frequency range. The third hydrodynamic mode cannot be seen in this figure since its magnitude is overshadowed by that of the structural modes. For the *z*-direction there are the two primary hydrodynamic modes in the lower frequencies which straddle a narrow structural peak between 200 and 300 Hz. Although the results are largely contaminated with Gaussian white noise, the lack of significant peaks in this plot are in agreement with the assumptions of the previous section in which it was identified that the vibration energy of the cylindrical structure should be predominantly radial, in the *x*-*y* plane, and that vibration in the *z*-direction can be neglected. Contrary to the vibration plots for the experiment vehicle, the outer-basket does not exhibit the higher-frequency vibrations but rather tends toward the lower end of the spectrum, which is expected due to having a greater physical mass in addition to being secured to the facility itself.

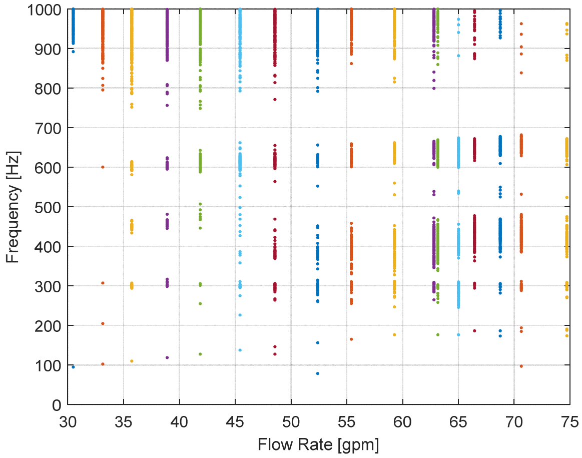

(VT-401x)

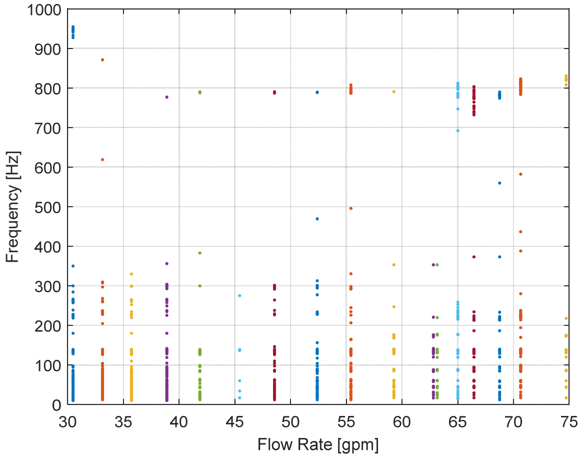

(VT-402x)

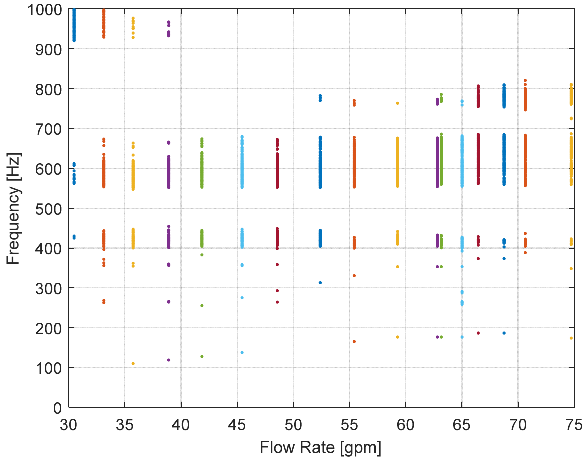

(VT-401y)

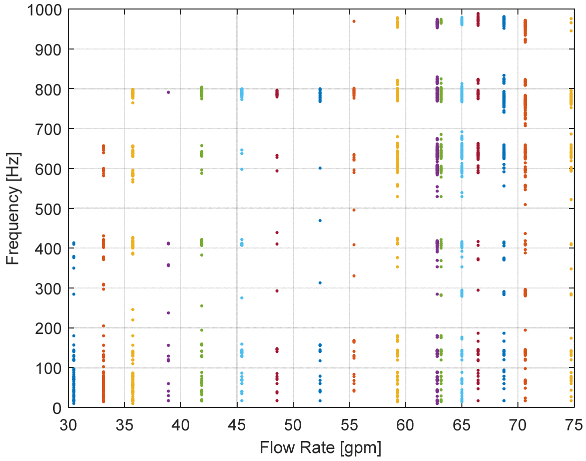

(VT-402y)

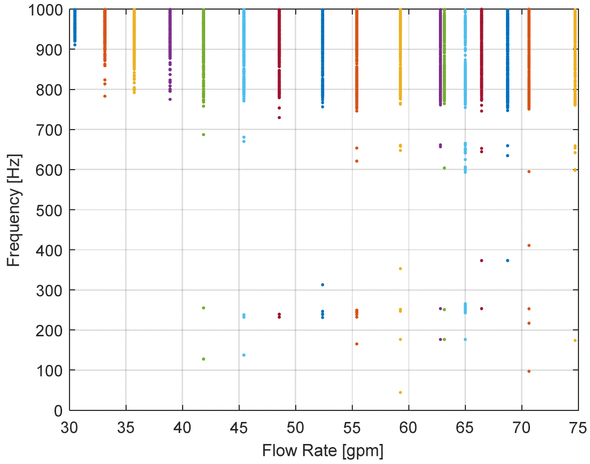

(VT-401z)

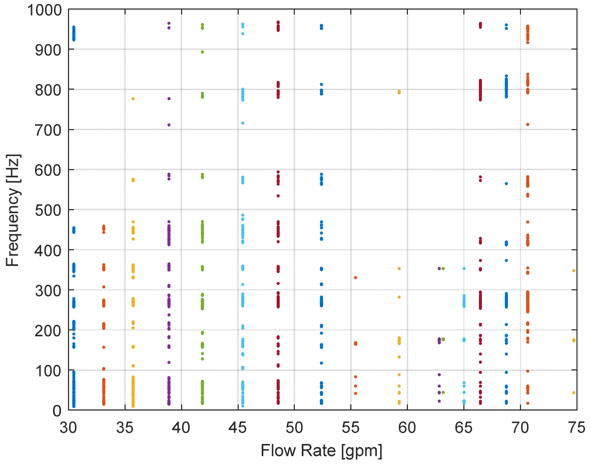

(VT-402z)

Fig. 16. 2σ peaks for VT-401 and VT-402 acceleration

Integrating the displacement using the methods laid out in [48] the resultant *x-y* displacement of the test element can be visualized through the orbital plots of Fig. 17. Noting that the axis are scaled to the millimeter range, the in-plane displacement of the test element is observed to be small in magnitude with the displacement of the flow simulator being even less. Most importantly, the general interference each respective solid-body does not appear to exhibit any coherent circumferential mode; from a safety basis this is beneficial since it suggests that the experiment will receive a uniform loading across the surface and not have excessive wear in any one particular location. It is also interesting to note that the magnitude of displacement slightly decreases at the highest flow rate, which is consistent with the information presented in Fig. 14; this is indicative that the hydrodynamic frequency modes contributes greatest to the displacement of the structure.

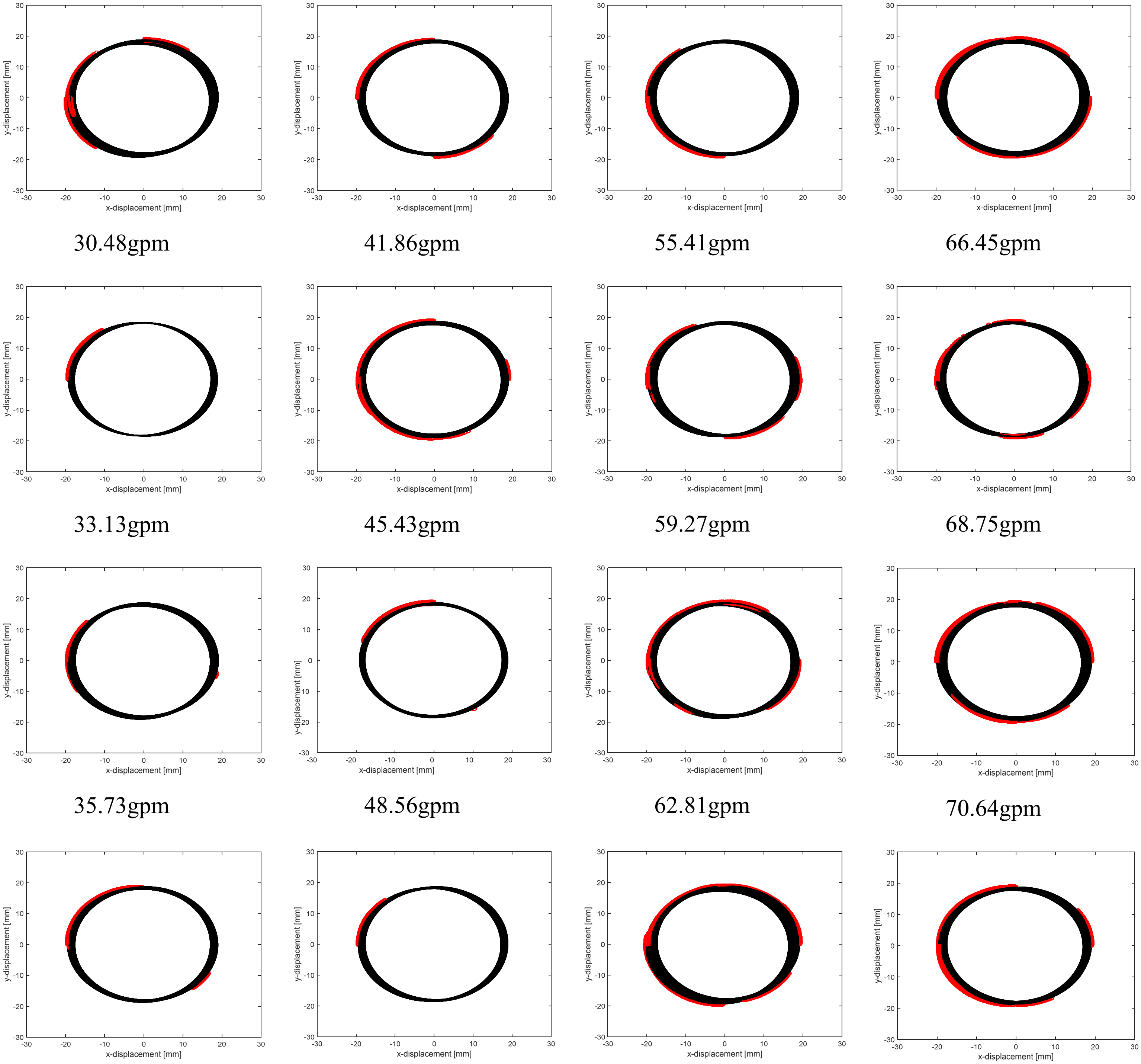

30.48gpm 41.86gpm 55.41gpm 66.45gpm

33.13gpm 45.43gpm 59.27gpm 68.75gpm

35.73gpm 48.56gpm 62.81gpm 70.64gpm

38.90gpm 52.39gpm 63.16gpm 74.72gpm

Fig. 17. *x-y* plane orbitals of test element vehicle and flow simulator (black) and their interference (red)

6 SUMMARY

A hydraulic testing campaign has been performed on an experiment referred to as the Mini-plate Large-B experiment which is intended on being placed in the Advanced Test Reactor for irradiation. The purpose of this testing campaign and study was to quantify, characterize and understand the structural response of the proposed in-pile experiment due to hydraulic loading prior to insertion in-reactor. Quantification of this information was accomplished through the simultaneous measurement of fluid characteristics including bulk flow rate, pressure drop, fluid temperature, and local pressure measurements (synthesized into local superficial velocity); accelerometers were mounted to discrete locations on different parts of the simulated in-pile experiment to acquire the motion profile of the multi-body system. Characterization of these measurements were accomplished by comparison of the vibrational information to a multi-body semi-numerical model (detailed herein), and showed that the hydraulic resident flow rates necessary to generate natural frequencies of the multi-body system are far higher than those experienced in this testing campaign as well as in the reactor; the frequencies observed by measurement would then be resultant of hydraulic loading explicitly (flutter, etc.). The accelerometer data was synthesized to provide both a frequency based understanding of the system wherein the multi-body system does not have any constructively interfering vibrational responses, but rather acts as two semi-independent systems. Furthermore, a spatial synthesis of the accelerometer measurements was made to understand whether local wear may occur due to localized vibrational bias in a particular direction within the multi-body system. While there was slight preference to the direction of motion, it was not observed to be significant in the hydraulic experiment to cause concern for the safety of mechanical integrity of the system in-pile

7 ACKNOWLEDGEMENTS

This work was supported by the U.S. Department of Energy, Office of Material Management and Minimization, National Nuclear Security Administration, under DOE-NE Idaho Operations Office contract DE-AC07-05ID14517. The authors would like to extend their gratitude to the reviewers of this manuscript for their insightful observations and suggestions. Their recommendations significantly improved the quality and content of this manuscript relative to its original form, and for that the authors are grateful. This information was prepared as an account of work sponsored by an agency of the U.S. Government. Neither the U.S. Government nor any agency thereof, nor any of their employees, makes any warranty, express or implied, or assumes any legal liability or responsibility for the accuracy, completeness, or usefulness of any information, apparatus, product, or process disclosed, or represents that its use would not infringe privately owned rights. References herein to any specific commercial product, process, or service by trade name, trademark, manufacturer, or otherwise, does not necessarily constitute or imply its endorsement, recommendation, or favoring by the U.S. Government or any agency thereof. The views and opinions of authors expressed herein do not necessarily state or reflect those of the U.S. Government or any agency thereof. Lastly, the authors would like to extend their gratitude to the reviewers of this document, for their critical review, this study resulted in far more thorough and significant outcomes.

BIBLIOGRAPHY

1. *GTRI: Reducing Nuclear Threats*. 2014.
2. *Hydro-Mechanical Fuel Test Facility*. 2015 [cited 2017 September 15]; Available from: http://ne.oregonstate.edu/hydro-mechanical-fuel-test-facility-hmftf.
3. Choi, J. and W.R. Marcum. *Prediction of Hydro-Mechanical Behavior In A Reactor Core with A Plate-Type Fuel Assembly*. 2013. WIT Press.
4. Marcum, W.R., et al., *The OSU Hydro-Mechanical Fuel Test Facility: Standard Fuel Element Testing*, in *International Meeting on Reduced Enrichment for Research and Test Reactors*. 2010: Lisbon, Portugal. p. 1-11.
5. Ribeiro, J.G.T. *Filtering in Frequency Domain to Avoid Time Aliasing*. in *IMAC-XX: A Conference on Structural Dynamics*. 2002. Los Angeles, California: Society for Experimental Mechanics.
6. Ribeiro, J.G.T., *Time Aliasing Induced Errors in Digital Double Integration.* 2013. **53**(9): p. 1689-1699.
7. Ribeiro, J.G.T. and J.T.P. De-Castro. *Using the FFT-DDI Method to Measure Displacements with Piezoelectric, Resistive and ICP Acceleromeers*. in *IMAC Conference & Exposition on Strcutral Dynamics*. 2003. Society for Experimental Mechanics.
8. Ribeiro, J.G.T., J.T.P. De-Castro, and J.L.F. Freire. *New Improvements in the Digital Double Integration Filtering Method to Measure Displacements Using Accelerometers*. in *International Modal Analysis Conference*. 2001. Kissimmee, Florida: Society for Experimental Mechanics.
9. Ribeiro, J.G.T., J.L.F. Freire, and J.T.P. De-Castro. *Problems in Analogue Double Integration to Determine Displacements from Acceleration Data*. in *International Modal Analysis Conference*. 1997. Orlando Florida: Society for Experimental Mechanics.
10. Ribeiro, J.G.T., J.L.F. Freire, and J.T.P. De-Castro. *Some Comments on Digital Integration Measure Displacements Using Accelerometers*. in *Internatioanl Modal Analysis Conference*. 1999. Kissimee Florida: Society for Experimental Mecahnics.
11. Smith, C.C., J.F. Dahl, and R.J. Thornhill, *The Duality of Leakage and Aliasing and Improved Digital Spectral Analysis Techniques.* Journal of Dynamic Systems, Measurement, and Control, 1996. **118**: p. 741-747.
12. Slifka, L.D., *An Accelerometer Based Approach to Measure Displacement of a Vehicle Body*, in *Department of Electrical and Computer Engineering*. 2004, University of Michigan: Ann Arbor, Michigan. p. 62.
13. Hayes, M.H., *Digital Signal processing*. First ed. Shaum's Outlines. 2011: McGraw-Hill Education.
14. Smith, S.W., *The Scientist & Engineer's Guide to Digital Signal Processing*. 1997: California Technical Publication.
15. Arraigada, M. and M. Partl. *Calculation of Displacements of Measured Accelerations, Analysis of Two Accelerometers and Application in Road Engineering*. in *6th Swiss Transport Research Conference*. 2006. Monte Verita, Ascona Switzerland: Institute for Economic Research.
16. Weisstein, E.W. *Newton-Cotes Formulas*. [cited 2017; Available from: http://mathworld.wolfram.com/Newton-CotesFormulas.html.
17. White, F.M., *Viscous Fluid Flow*. Third Edition ed. 2005: McGraw-Hill Education.

18. Chen, S.S., *Flow-Induced Vibration of Circular Cylindrical Structures*, C.T. Division, Editor. 1985, Argonne National Laboratory: Argonne, Illinois. p. 1-619.
19. *White Paper: San Onofre Nuclear Plant Replacement Steam Generators*. 2013, Southern California Edison. p. 1-11.
20. Stokes, G.G., *On the Effect of the Internal Friction of Fluids on the Motion of Pendulums.* Transactions of the Cambridge Philosophical Society, 1850. **9**: p. 1-86.
21. Chen, S.S. and H. Chung, *Design Guide for Calculating Hydrodynamic Mass Part I. Circular Cylindrical Structures*, C.T. Division, Editor. 1976, Argonne National Laboratory: Argonne, Illinois.
22. Fritz, R.J. and E. Kiss, *The Vibration Response of a Cantilevered Cylinder Surrounded by an Annular Fluid*. 1966, Knolls Atomic Power Laboratory: Schenectady, New York.
23. Fritz, R.J., *The Effect of Liquids on the Dynamic Motions of Immersed Solids.* Journal of Engineering for Industry, 1972. **94**(1): p. 167-173.
24. Beskos, D.E., *Statics and Dynamics of Shells*, in *Boundary Element Analysis of Plates and Shells*, D.E. Beskos, Editor. 1991, Springer. p. 93-140.
25. Flugge, W., *Stresses in Shells*. 1960: Springer.
26. Amabili, M., F. Pellicano, and M.P. Paidoussis, *Non-Linear Dynamics and Stability of Circular Cylindrical Shells Containing Flowing Fluid. Part I: Stability.* Journal of Sound and Vibration, 1999. **225**(4): p. 655-699.
27. Amabili, M., F. Pellicano, and M.P. Paidoussis, *Non-Linear Dynamics and Stability of Circular Cylindrical Shells Containing Flowing Fluid. Part II: Large-Amplitude Vibrations Without Flow.* Journal of Sound and Vibration, 1999. **228**(5): p. 1103-1124.
28. Amabili, M., F. Pellicano, and M.P. Paidoussis, *Non-Linear Dynamics and Stability of Circular Cylindrical Shells Containing Flowing Fluid. Part III: Truncation Effect Without Flow and Experiments.* Journal of Sound and Vibration, 2000. **237**(4): p. 617-640.
29. Amabili, M., F. Pellicano, and M.P. Paidoussis, *Non-Linear Dynamics and Stability of Circular Cylindrical Shells Containing Flowing Fluid. Part IV: Large-Amplitude Vibrations with Flow.* Journal of Sound and Vibration, 2000. **237**(4): p. 641-666.
30. Lee, L.T. and J.C. Lu, *Free Vibration of Cylindrical Shells Filled with Liquid.* Computers and Structures, 1995. **54**(5): p. 997-1001.
31. Weisstein, E.W. *Galerkin Method*. Available from: http://mathworld.wolfram.com/GalerkinMethod.html.
32. Chen, S.S. and G.S. Rosenberg, *Free Vibrations of Fluid-Conveying Cylindrical Shells.* Journal of Engineering for Industry, 1974. **96**(2): p. 420-426.
33. Kraus, H., *Thin Elastic Shells*. 1968: Wiley.
34. Chen, S.S. and G.S. Rosenberg, *Dynamics of a Coupled Shell-Fluid System.* Nuclear Engineering and Design, 1975. **32**(3): p. 302-310.
35. Krajcinovic, D., *Vibrations of Two Coaxial Cylindrical Shells Containing Fluid.* Nuclear Engineering and Design, 1974. **30**: p. 242-248.
36. Au-Yang, M.K., *Free Vibration of Fluid-Coupled Coaxial Cylindrical Shells of Different Lengths.* Journal of Applied Mechanics, 1976. **43**(3): p. 480-484.
37. Naudascher, E. and D. Rockwell, *Flow-Induced Vibrations: An Engineering Guide*. 1994, Mineola, New York: Dover Publications, Inc.
38. Paidoussis, M.P. and C. Helleur, *On Ovalling Oscillation of Cylindrical Shells in Cross-Flow.* Journal of Sound and Vibration, 1979. **63**(4): p. 527-542.

39. Dockstader, E.A. and W.F. Swiger. *Resonant Vibration of Steel Stacks*. 1956. American Society of Civil Engineers.
40. Johns, D.J. and C.B. Sharma, *On the Mechanism of Wind-Excited Ovalling Vibrations of Thin Circular Cylindrical Shells*, in *Flow-Induced Structural Vibrations*. 1974, Springer. p. 650.
41. Paidoussis, M.P., *Dynamic Stability of Pipes Conveying Fluid.* Journal of Sound and Vibration, 1974. **33**(3): p. 267-294.
42. Woolstenhulme, N.E., et al., *Design of Irradiation tests for Monolithic Fuel Qualification*, in *36th International Meeting on Reduced Enrichment for Research and Test Reactors*. 2015: Seoul, South Korea. p. 1-10.
43. Marcum, W., A. Weiss, and B. Woods, *Miniplate, Large-B Flow Tests - Matrix Test Plan, Revision 1*, D.o.N.E.a.R.H. Physics, Editor. 2014, Oregon State University: Corvallis Oregon. p. 1-46.
44. Paidoussis, M.P. and J.P. Denise, *Flutter of Thin Cylindrical Shells Conveying Fluid.* Journal of Sound and Vibration, 1972. **20**(1): p. 9-26.
45. Mohd-Yasin, F., C.E. Korman, and D.J. Nagel, *Measurement of Noise Characteristics of MEMS Accelerometers.* Solid-State Electronics, 2003. **47**(2): p. 357-360.
46. Renfer, A., et al., *Vortex Shedding from Confined Micropin Arrays.* Microfluidics and Nanofluidics, 2013. **15**(2): p. 231-242.
47. Guillaume, D.W. and J.C. LaRue, *Comparison of the Vortex Shedding Behavior of a Single Plate and a Plate Array.* Experiments in Fluids, 2001. **30**(1): p. 22-26.
48. Latimer, G., *Vibration Analysis of Advanced Test Reactor Miniplate Hydraulic Test*, in *School of Nuclear Science and Engineering*. 2016, Oregon State University: Corvallis Oregon. p. 143.